OPTICAL PROPERTIES OF CRYSTALS OF THALLIUM COMPOUNDS $TlMeX_2$ (Me = Ga, In; X = S, Se)

タリウム化合物 $TlMeX_2$ (Me=Ga,In; X=S,Se) 結晶の光学的特性

BY

PAUCAR RAMOS RAUL JULIO

A THESIS SUBMITTED TO

THE DEPARTMENT OF ENGINEERING

IN PARTIAL FULLFILLMENT OF THE REQUIREMENTS FOR THE DEGREE

OF

DOCTOR OF ENGINEERING

IN

CHIBA INSTITUTE OF TECHNOLOGY

MARCH 2017

ABSTRACT

Ternary thallium dichalcogenide compounds with the chemical formula $TlMeX_2$ (Me = In, Ga; X = Se, S, Te) are a family of low-dimensional semiconductors that possess both layered ($TlInS_2$, $TlGaS_2$, and $TlGaSe_2$) and chain-like ($TlInSe_2$, $TlInTe_2$, and $TlGaTe_2$) structures. Upon cooling, $TlMeX_2$ exhibits a sequence of structural phase transitions from a paraelectric-normal (N) phase to a ferroelectric-commensurate (C) phase via an intermediate incommensurate (I) phase. These compounds have remarkable characteristics in each structural phase. In the paraelectric-N phase, these compounds exhibit nonlinear current–voltage (*I–V*) characteristics and a high degree of anisotropy. Moreover, $TlGaSe_2$ semiconductor compounds are extensively used in X-ray detectors owing to their wide bandgap. In the I-phase, thallium atoms are not an integral multiple of the lattice, and therefore the crystal lattice has an inconsistent modulation period. This modulation is known as nano-spatial modulation. Moreover, in the C phase, ternary thallium dichalcogenide compounds have potential applicability in ferroelectric devices. Furthermore, it has been reported that $TlInS_2$, $TlInTe_2$ and $TlInSe_2$ exhibits a high Seebeck coefficient (i.e., $TlInSe_2$ exhibits 10^6 μV/K) at a temperature below 150 K, which shows that these compounds could be used as a thermoelectric conversion material. Upon laser light irradiation of a $TlMeX_2$ chain-like structure, a macroscopic change in the structure was discovered in 2008. This phenomenon could be used for optical drive actuators without the need for wiring, even in significantly weak light of 1 W/cm^2. This feature could also be applied to micro electro mechanical systems (MEMSs) as a part of a micromachine driver such as a microactuator operated with low light energy. However, even thorough many investigations have been performed on the physical properties of layered $TlMeX_2$ crystals, there is still controversy regarding the interpretation of these properties. Moreover, the mechanisms that lead to the phase transitions are unclear partly because of the existence of different polytypes.

The aim of this study was to study the relationship between the optical properties of layered ternary thallium chalcogenide crystals and their structural phase transitions. In this study, the photoluminescence (PL) spectrum at the band-edge region measured using a confocal microscopy system was examined by excitation density dependence at

77 K and over a temperature range 77–300 K, which includes the range of successive phase transitions. Moreover, the temperature dependence of the Raman spectra in single-crystal $TlInS_2$ obtained from the polarized Raman spectra in the low-frequency region was explored. In general, it is believed that phase transitions in $TlInS_2$ and $TlGaSe_2$ compounds are associated with the displacements of Tl atoms. Owing to the heavy weight of the Tl atom, the low-frequency region in the Raman spectra of $TlInS_2$ is, therefore, of particular interest.

We examined the PL spectra of $TlInS_2$ crystals using a confocal microscopy system. For light polarization $\boldsymbol{E}\perp\boldsymbol{c}^*(\boldsymbol{k}//\boldsymbol{c}^*)$, a strong PL band was observed in the temperature range of 77 to 300 K, over which a series of phase transitions occurred. At 77 K (ferroelectric-C phase) and under an excitation density greater than 0.1 MW/cm^2, the PL spectrum consisted of two components: (1) free-exciton (*H* band) luminescence and (2) biexciton luminescence (*M* band). The binding energy of the biexciton luminescence is estimated to be ~13.5 meV, and the structure dissociated at 160 K. For temperatures higher than 300 K, the crystal phase underwent a transition to a paraelectric-N phase through an intermediate I phase, and the PL spectra mainly consisted of *H* band emission. To the best of our knowledge, this is the first observation of biexcitonic emission in the PL spectra of $TlInS_2$ crystals.

Furthermore, we examined the PL spectra of $TlGaSe_2$ using confocal microscopy. The PL spectra apparently appeared only for the $\boldsymbol{k}\perp\boldsymbol{c}^*$ configuration. The asymmetric spectra were separated into two Gaussian peaks, A and B, located at 2.01 eV and 2.10 eV, respectively. By examining the excitation intensity dependence of the PL intensity and comparing the results to previously reported data, we assigned peak B to proper free excitons emitted from the $TlGaSe_2$ crystals. To the best of our knowledge, this is the first observation of free excitons in $TlGaSe_2$ using PL measurements. Peak A was also assigned to free excitons. However, it is possible that the peak A free-exciton emission came from crystals in which the ***a*** and ***b*** axis were mixed and exchanged or from layers that were stacked with a parallel shift.

For layered $TlInS_2$ and $TlGaSe_2$, Raman spectra in the frequency region of 35–400 cm^{-1} were studied over the temperature range of 77–300 K. The observed lines in the Raman spectra were deconvoluted into Lorentzian peaks, and the temperature

dependence of each peak's parameters, i.e., peak position and full width at half maximum (FWHM), were obtained. The irregular behavior of the temperature dependence of the Lorentzian parameters is reported herein. The reason for the appearance and disappearance of Raman modes and the irregular behavior of the temperature dependence of the Lorentzian parameters may be a structural phase transition. A result of this transition is the quadrupled in ferroelectric-C phase along the crystallographic $\boldsymbol{c}$*-axis. This phenomenon is known as superlattice.

Moreover, we identified the symmetry modes for the $TlInS_2$ crystal. The Raman spectra shows 12 phonon modes in the $\boldsymbol{x(zz)\bar{x}}$ geometry, while 15 modes in $\boldsymbol{x(yz)\bar{x}}$. In total, we observed 19 phonons, three more than those previously reported for the same frequency range at 300 K. The small number of observed phonon modes is in agreement with the supposition that the space group of the crystal is $\boldsymbol{C_{2h}^6}$. In this hypothesis, group theoretical analysis gives 24 Raman active modes (10 A_g +14 B_g) at the center of the Brillouin zone. Thus, we observed all of the 10 A_g phonons and nine of the 14 B_g phonons predicted. In addition, we studied the polarized Raman spectra of $TlInS_2$ crystals across a wide temperature range that included the reported region of the N-I-C transition. In the $\boldsymbol{x(zz)\bar{x}}$ geometry, we identified three Raman modes that are possibly related to the interlayer bonding between Tl and S atoms and four Raman modes that may be associated to the intralayer bonding between In and S atoms.

要旨

三元タリウム系化合物$TlMeX_2$（Me ： In, Ga,　X: S, Se, Te)は低次元構造である擬一次元又は擬二次元結晶構造をもつ物質である。この物質は温度が低下するにつれて常誘電相（ノーマル相）⇒中間相（インコメンシュレート・不整合相）⇒強誘電相(コメンシュレート相)へと構造相転移を示す。それぞれの相に特徴ある構造特性をもち、物理的に興味のある材料であるだけでなくデバイスへの応用も期待されている。常誘電相では、三元タリウム系化合物は特異な電流電圧(I-V)特性をもつ異方性の高い半導体である。また、$TlGaSe_2$ ではワイドギャップ半導体であるため放射線検出器として応用されている。インコメンシュレート相では、タリウム原子が格子の整数倍ではない、結晶格子と不整合な変調周期をもっており、この変調をナノ空間変調構造と呼んでいる。このナノ空間変調構造に起因した光誘起メモリー効果の発現や光学異方性の変化などの特異な物性が報告されていることから、光学素子や光でデータの記録・読み出しを行うことができる光メモリーなどへ応用できる可能性がある。また、$TlInSe_2$ では150 ℃以下において約$10^6\,\mu V/K$ もの大きなゼーベック係数を示すことも報告されており、熱電変換材料としての可能性もある。さらに、コメンシュレート相では、強誘電体材料としてデバイスへの応用も期待されている。2008 年には、本研究グループの大串・岸杭らよって鎖状構造$TlMeX_2$ である$TlInSe_2$ 及び$TlGaTe_2$ においてレーザー光照射によるマクロな表面形状変化を発見し、また、光学顕微鏡による直接観測にも成功した。この現象は、光を用いるため配線の必要がなく空間制御が容易である事から光駆動アクチュエータへの応用が考えられる。本現象が1　W/cm^2 程の極めて弱い光でも確認出来る。ことから、小さな光エネルギーで動作可能なマイクロアクチュエータとしてマイクロマシンの駆動部としてMEMS（Micro Electro Mechanical System）の分野へ応用できる可能性がある。

一方で、70年代 から三元タリウム系化合物について、いくつかの圧力及び温度条件で、様々な実験方法（X線回折、中性子散乱、赤外分光法、ラマン散乱光法、フォトルミネセンス光法など）を用いて、多くの研究をされている。しかしながら、三元タリウム系化合物の多くは未だその基礎的な物性が明らかになっていない。具体的にはその基礎物性と構造相転移との関係については十分理解されていない。更に、それぞれの研究では、異なる結晶構造であるポリタイプや純度の高くない単結晶を用いていため、いくつかの論争が過去に起きたことがある。したがって、結晶性や純度が高い三元タリウム系化合物を用いて基礎的な物性と相転移との関係を統一的に研究することが必要とされている。この研究には、最先端設備である共焦点顕微システムを用いて三元タリウム系化合物に属する擬二次元結晶構造である$TlInS_2$や$TlGaSe_2$の結晶構造および光学的特性について解明することを目的として研究を行った。アゼルバイジャン物理大学との研究共同として、アゼルバイジャン物理学研究所にてブリッジマンストックバーガー法により$TlInS_2$や$TlGaSe_2$の純度の高いバルク単結晶が製作された。そして千葉工業大学にて、結晶構造や光学的特性について解明するため

共焦点顕微システムを用いて分光法実験（フォトルミネッセンスおよび非偏光または偏光ラマン散乱など）を行った。以下、本研究で得られた知見をまとめる。

- $TlInS_2$や$TlGaSe_2$におけるエネルギーバンドと構造相転移との関係について検討するためにフォトルミネセンスを測定し解析した。

  - $TlInS_2$ では、測定温度77 Kでバンド端付近に非常に強度の強い発光を観測した。観測した発光スペクトルをローレンツ関数を用いて2つのピーク（M: 2.507 eV, H: 2.52 eV）に分離した。励起強度依存性の解析から、両ピークの挙動が異なりピークMの強度はピークHの強度の2乗倍に比例することからピークMは励起子分子、ピークHは自由励起子によると同定した。本研究において初めてフォトルミネセンス測定による$TlInS_2$ の励起子分子発光を観測した。

  - $TlGaSe_2$ では測定温度77 Kにおいてバンド端付近で明確な発光を観測した。この発光スペクトルをガウス関数を用いてピークエネルギーが2.01 eV であるピークA と2.10 eV であるピークB の二つの波形に分離した。また励起強度依存性の解析から、両ピークは同一の挙動を示すことからピークA とピークB はともに自由励起子による発光であると同定した。PL 測定による$TlGaSe_2$ の自由励起子の観測は、本研究が初めてである。しかしながら、ピークA の自由励起子発光は、結晶のa 軸とb 軸が混在して積層された、もしくは平行にずれて積層された不完全な結晶層による発光の可能性がある。

- $TlInS_2$や$TlGaSe_2$の結晶構造と構造相転移との関係について検討するためにラマン散乱スペクトルの測定を行い解析した。

  - $TlGaSe_2$ では、構造相転移温度領域付近についてラマンスペクトルについて詳しく解析を行った。一部のフォノンピークに関しては温度の上昇によりラマンシフトが異常な振る舞いを示し、構造相転移が原因であると考えられる。

  - $TlInS_2$ では、構造相転移温度領域付近についてラマンスペクトルについて詳しく解析を行った。一部のフォノンピークに関しては温度の上昇によりラマンシフトが異常な振る舞いを示し、構造相転移が原因であると考えられる。または、構造相転移温度付近における偏光ラマン散乱スペクトルの温度依存性について調べた。その結果、フォノンピークが温度に敏感に変化するモードとそうでないモードを分離し、それぞれの起源が結晶層間および結晶層内の分子結合によると分類した。

最後にすべての実験結果をまとめて本研究で明らかになった点を総括し、今後の課題について述べる。

TABLE OF CONTENTS

CHAPTER 1

Introduction

Ternary thallium dichalcogenide compounds with the chemical formula $TlMeX_2$, where Me is a group-III metal (In or Ga) and X is a group-IV (chalcogenide) element (Se, S, or Te), are a family of low-dimensional semiconductors that have both quasi-one-dimensional chain-like ($TlInSe_2$, $TlInTe_2$, and $TlGaTe_2$) and quasi-two-dimensional layered ($TlInS_2$, $TlGaS_2$, and $TlGaSe_2$) structures [1–9]. These compounds have been attracting increasing interest because of their electrical, optical, and structural properties and thus show potential for optoelectronics applications [10–24].

In this thesis, we focus on $TlInS_2$ and $TlGaSe_2$ crystals, which belong to the class of ternary thallium dichalcogenide compounds with layered structures. In Chapter 1, we discuss the structural and physical properties and potential applications of these compounds. We also examine the photoluminescence and Raman spectroscopy studies of $TlInS_2$ and $TlGaSe_2$ compounds performed so far. Finally, we present and explain the purpose of this study.

1.1 Structural properties

1.1.1 Crystal structure at ambient conditions

Room-temperature X-ray diffraction (XRD) measurements [2, 4, 7–9] have shown that $TlMeX_2$ compounds (where MeX_2 = InS_2, $GaSe_2$, GaS_2) are iso-structural layered crystals. These compounds crystallize in the monoclinic system with a centrosymmetric space group, $C2/c$, which is referred to as the normal (N) phase [2, 4]. The monoclinic crystal system is shown in Figure 1.1 and the structural parameters of the layered $TlMeX_2$ compounds are summarized in Table 1.1.

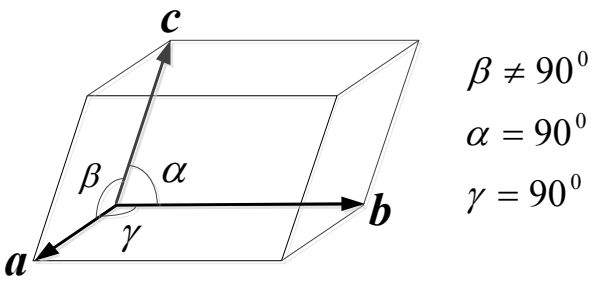

Figure 1.1 The monoclinic crystal system.

Table 1.1: Structures of layered compounds at ambient conditions.

Compound	Structure	Space group	*a* (Å)	*b* (Å)	*c* (Å)	*β*	Ref.
$TlInS_2$	monoclinic	C_{2h}^6 - C2/c	10.90	10.94	15.18	100.21°	[4, 7]
$TlGaSe_2$	monoclinic	C_{2h}^6 - C2/c	10.772	10.771	15.363	100.6°	[2, 4, 9]
$TlGaS_2$	monoclinic	C_{2h}^6 - C2/c	10.299	10.284	15.175	99.63°	[4, 8]

The quasi-two-dimensional structure consists of strictly periodic layers parallel to the (001) plane, which coincides with the ***ab*** plane. The fundamental structural unit of a layer is an Me_4X_{10} tetrahedron built in an adamantine-like configuration by four elementary MeX_4 tetrahedra with common corners. The combination of these tetrahedrons to form a layer results in trigonal prismatic voids. The Tl^+ ions are positioned in these trigonal prisms between the layers and are arranged in straight lines parallel to the [110] and $[1\bar{1}0]$ directions, which correspond to the ***a*** and ***b*** crystallographic axes, respectively. Each successive layer is rotated 90° from the normal of the previous layer [2, 4]. Figure 1.2 shows the tetrahedra, tetrahedron, simplified representation of the tetrahedron, and combination of the tetrahedrons to form a layer. Figure 1.3 shows a schematic of the layered structure of the $TlMeX_2$ compounds, where ***c**** is the axis perpendicular to the (001) plane.

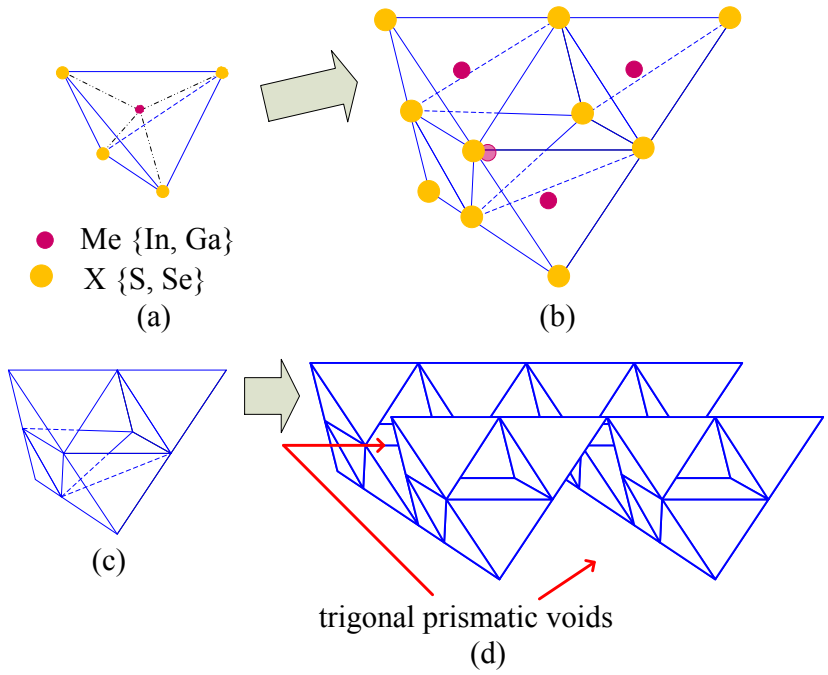

Figure 1.2 (a) MeX_4 tetrahedra. (b) Me_4X_{10} tetrahedron, (c) simplified representation of the tetrahedron shown in (b), and (d) combination of tetrahedrons shown in (c) to form a layer.

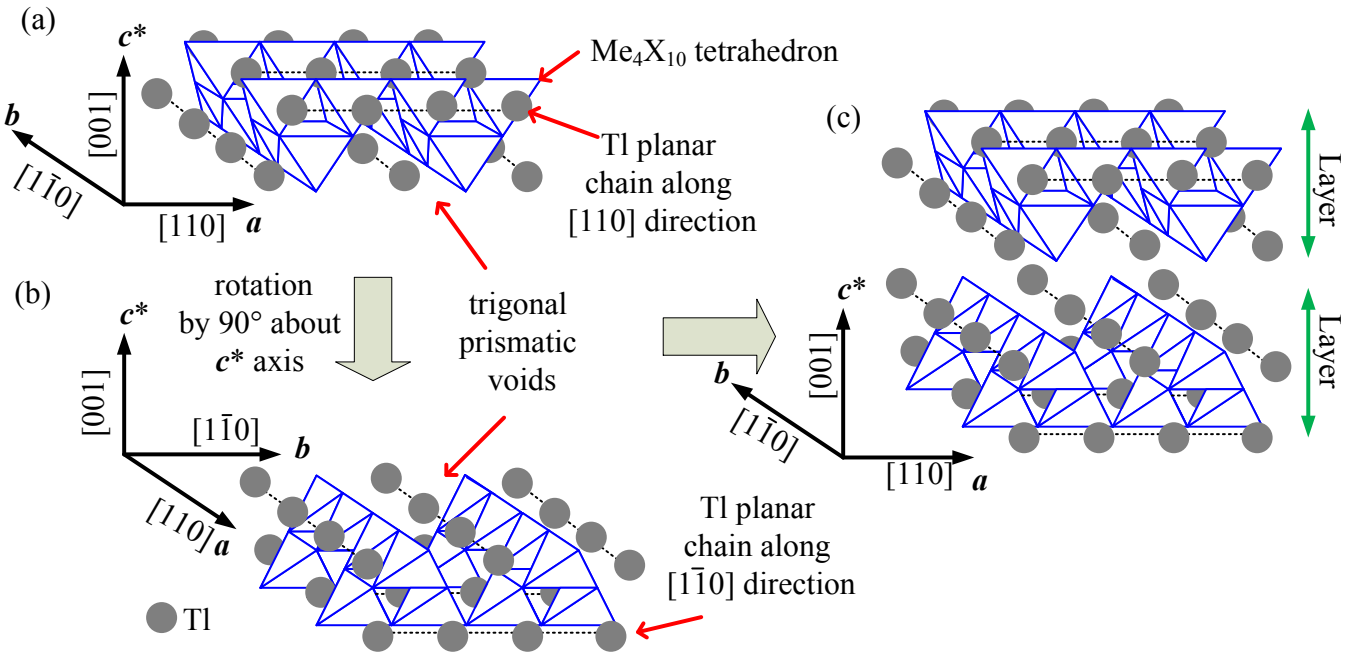

Figure 1.3 (a) Schematic of the combination of tetrahedrons and Tl^+ ions in a layer. The Tl^+ ions are positioned in trigonal prismatics voids between the layers arranged in straight lines parallel to the ***a*** [110] and ***b*** $[1\bar{1}0]$ axes. (b) Layer obtained through a rotation of 90° about the ***c**** axis of the layer shown in (a). (c) Layered structure of the $TlMeX_2$ compounds.

In most of these layered crystals, strong ionic-covalent chemical bonds are present inside the layers (intralayer bonding), whereas the interactions between the layers (interlayer bonding) are very weak and are usually described as van der Waals interactions [4, 20]. In the $TlMeX_2$ layered compounds, interlayer bonding occurs between Tl and X atoms, whereas intralayer bonding appears between Me and X atoms. Figure 1.4 shows a projection of the structure on the ***ac**** plane [25–27]. Intralayer (1) and interlayer (2) bonding are also shown.

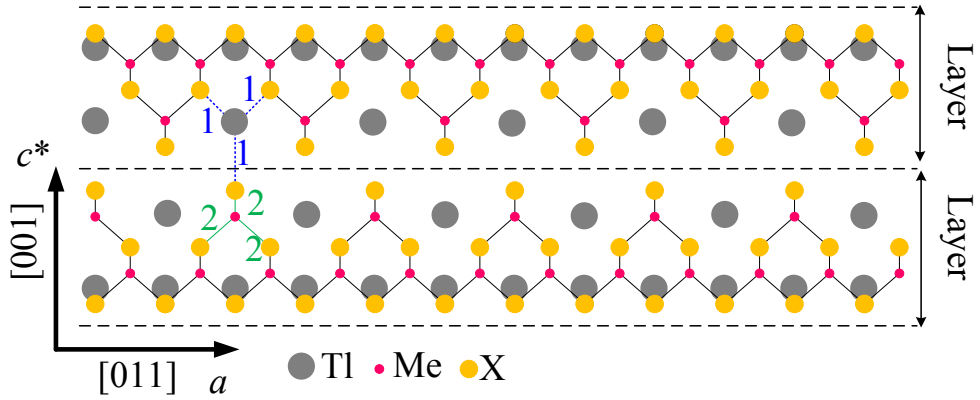

Figure 1.4 Projection of the $TlMeX_2$ compound structure on the ***ac**** plane. (1) Interlayers (van der Waals) bonding between Tl and X atoms and (2) intralayer (ionic-covalent) bonding between Me and X atoms.

1.2.1 Structural phase transition

Structural phase transitions in $TlInS_2$ ware discovered in the 1980s by Volkov et al. [28], Aliev et al. [30], and Vakhrushev et al. [31], who observed the anomalous behavior of this compound by means of dielectric, optical-dielectric, and dilatometric and neutron diffraction measurements, respectively [22]. Since then, these phase transitions have been studied by other authors [20, 22, 28–38] using many experimental techniques, such as heat capacity, dielectric, X-ray, neutron diffraction, and spectroscopy measurements. Currently, it is well accepted that upon cooling, $TlMeX_2$ compounds exhibit a temperature dependent sequence of structural phase transitions from a paraelectric-normal (N) phase to a ferroelectric-commensurate (C) phase via an intermediate incommensurate (I) phase. Here, we use the following standard designations to refer to these temperature-dependent phase transitions: *Ti* correspond to the high-temperature N-to-I phase transition and *Tc* to the low-temperature "lock-in" I-to-C phase transition [20, 22]. According to the experimental results of different authors,

the temperature *Ti* and *Tc* can vary slightly from crystal to crystal. In this work, we will consider the temperatures indicated in Table 1.2, which are accepted by most researchers. However, for $TlGaS_2$ these transitions are not as pronounced as for $TlInS_2$ and $TlGaSe_2$ in a narrow temperature range.

Two principally different structural deformation mechanisms have been proposed for paraelectric-ferroelectric transitions in layered $TlMeX_2$: (1) angular deformations in the MeX_4 tetrahedra [33] and (2) slippage of Tl^+ atoms channels in the [110] and $[1\bar{1}0]$ directions on the ***ab*** plane [6, 34]. According to [39], the origin of the phase transition in $TlGaS_2$ could be attributed to the first mechanism, while the second mechanism occurs in the case of $TlInS_2$ and $TlGaSe_2$. Moreover, owing to these transitions, the unit cell in the ferroelectric-C phase is quadrupled (i.e., the unit cell of the ferroelectric phase is four times the cell of the paraelectric phase) along the crystallographic ***c*** axis. Additionally, the transitions are accompanied by anomalies in the dielectric susceptibility [36, 38], heat capacity [40, 41], and linear expansion coefficient [42–44]. Figure 1.5 shows a simplified view of these temperature-induced structural phase transitions at constant pressure.

Table 1.2: High-temperature (*Ti*) N-to-I phase transition and low-temperature (*Tc*) "lock-in" I-to-C phase transition. For more information on the method of investigation (determination) of temperatures *Ti* and *Tc*, see Tables 18, 19, and 20 of reference [20].

Laminar compound	***Ti* (K)** **N-to-I** **phase transition**	***Tc* (K)** **I-to-C** **phase transition**
$TlInS_2$	216	200
$TlGaSe_2$	120	107
$TlGaS_2$	250	180

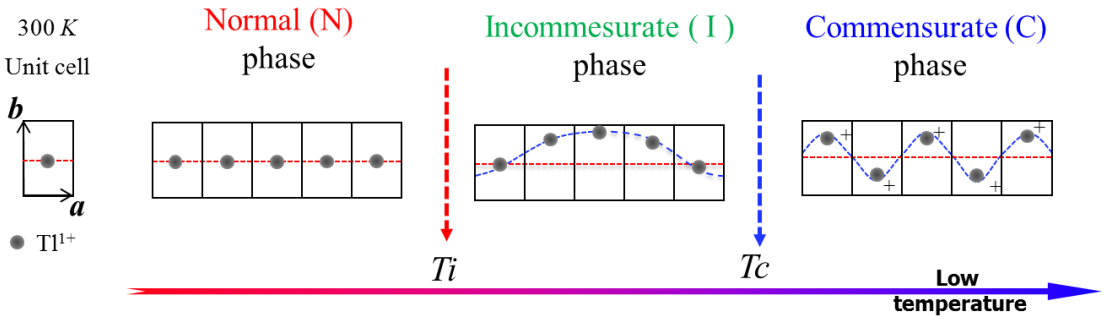

Figure 1.5 Simplified view of the temperature-induced structural phase transitions in $TlMeX_2$ compounds at constant pressure.

1.2 Physical properties and potential applications

Layered $TlMeX_2$ compounds have attracted particular interest because their unique structural and physical properties and their potential for application in optoelectronics [10–24]. These compounds exhibit a wide bandgap (see Table 1.3), photoconducting and semiconducting behavior, and a high degree of anisotropy in their physical properties (i.e., conductivity, linear expansion coefficient, and dielectric function) parallelly and perpendicularly to the crystal layer plane. Furthermore, these compounds exhibit remarkable characteristics in each structural phase. In the N phase, $TlInS_2$ [22] and $TlGaSe_2$ [23, 24] compounds are promising materials for the constructions of X-ray and γ-ray detectors owing to their wide band gap and appropriate mobility-lifetime product. In the I phase, layered $TlInS_2$ compounds doped with impurities (Fe, Mn, Cr, and Ge) lead to a rapid relaxation of the dielectric susceptibility. This behavior (known as relaxor) is caused by the formation of polar nano-regions (nanodomains) [22]. Similar relaxor behavior has also been observed in the γ-irradiated $TlInS_2$ compounds [47].

Moreover, in the C phase, ternary thallium dichalcogenide compounds have potential applicability in ferroelectric devices. The considerable scientific interest by researches in ferroelectric materials with smeared phase transitions stems from the fact that these materials are very promising for uses in data storage systems [47].

Furthermore, it has been reported [10, 15] that $TlInS_2$, $TlInSe_2$ and $TlInTe_2$ exhibit a high Seebeck coefficient (i.e,, $TlInSe_2$ exhibits 10^6 μV/K) at a temperature below 150 °C, which shows that these compounds could be used as thermoelectric conversion materials. Moreover, a strong photoacoustic effect has been observed upon irradiation of layered $TlGaSe_2$ with weak nanosecond laser pulses [48]. This phenomenon showed an acoustic pulse amplitude ten times higher when the exciting pump beam was parallel to the ***c*** axis of the crystal than when it was perpendicular to ***c***. Such effects allow wide range of applications (i.e., sonar detection, underwater communications lines, optical switches, and novel selective radiation detectors) [22].

Table 1.3: Optical bandgap at 300 K, where E_g^d and E_g^i(eV) are the direct and indirect bandgap energies, respectively.

Laminar compound	E_g^d**(eV)**	E_g^i**(eV)**
$TlInS_2$	2.33 [11]	2.28 [11]
$TlGaSe_2$	2.11 [12] 2.23 [45]	1.83 [12] 2.03 [45]
$TlGaS_2$	2.53 [12] 2.54 [46]	2.38 [12] 2.46 [46]

However, although many studies have been performed on the properties of layered $TlMeX_2$ crystals, there is still controversy regarding the interpretation of these properties. Moreover, the mechanisms that lead to the phase transitions are still unclear partly because of the existence of different polytypes [49–52]. At present, five crystal modifications of the $TlInS_2$ compound are known [49]: monoclinic, triclinic, tetragonal, hexagonal, and orthorhombic. Furthermore, the monoclinic $TlInS_2$ and $TlGaSe_2$ have several polytype modifications that differ in the ***c*** lattice parameter: ***c***', 2***c***', 3***c***', 4***c***', …. whereas parameters ***a*** and ***b*** change only slightly with increasing ***c*** [49–52].

1.3 Photoluminescence and Raman spectroscopy

1.3.1 Photoluminescence studies of $TlInS_2$ and $TlGaSe_2$

Figure 1.6 shows the results of early studies near the fundamental band edge by transmissions, reflections, ellipsometry, and photoluminescence (PL) measurements in $TlInS_2$. Label (1) corresponds experimental results obtained by means of transmission and reflection measurements in $TlInS_2$ crystals using an incident beam of unpolarized light normal to the (001) plane, that is, the $\boldsymbol{E}\perp\boldsymbol{c}^*(\boldsymbol{k}//\boldsymbol{c}^*)$ configuration ($\boldsymbol{E}$ is the electrical vector of the incident light, $\boldsymbol{k}$ is the propagation direction of the incident beams, and $\boldsymbol{c}^*$ is the axis perpendicular to the $\boldsymbol{ab}$ plane). Then, the relationship of the bandgap (E_g) and free-exciton (E_{FE}) energies with the temperature was obtained using the Bose-Einstein statistical factor [53].

$$E_g(\mathrm{T}) = E_B - \alpha_B \left[1 + \frac{2}{e^{\theta_B/\mathrm{T}} - 1}\right] \qquad (1.1)$$

$$E_{FE}(\mathrm{T}) = E_g(\mathrm{T}) - E_i \qquad (1.2)$$

where E_B and α_B are fitting parameters, Θ_B is the average temperature (Einstein characteristic temperature) of phonons interacting with the electronic subsystem, and E_i is the activation energy (binding energy) of the excitons [53, 54].

Labels (2), (3), and (4) in Figure 1.6 are the energy positions of the PL peaks obtained from the temperature dependence of the photoluminescence spectra of the $TlInS_2$ crystal [55–57]. At low temperatures, in the $\boldsymbol{E}\perp\boldsymbol{c}^*(\boldsymbol{k}//\mathbf{c}^*)$ configuration, the PL spectra of $TlInS_2$ show two PL bands, a low-intensity band at the low-energy side (2.1–2.3 eV) [57] and a high-intensity band at the high-energy side (2.3–2.6 eV) [55, 56]. The low-intensity band have been attributed to radiative donor-acceptor pair (DAP) recombination [57], whereas the recombination mechanism of the high-intensity band (denoted as *H* band in early studies) have been assigned to excitonic emission [55, 56].

Some differences arise when comparing the results of these early studies. The energy position obtained by Equation 1.2 [53] shows the best agreement with the

excitonic *H* band emission obtained experimentally at low temperatures (C phase), whereas the energy positions of the *H* bands and E_{FE} reveal a significant deviation in the I and N phase. Therefore, the Bose-Einstein statistical treatment may not be adequate in the extended temperature range of N-I-C phase transitions. Moreover, in early PL studies, the differences in the obtained energy values for the *H* band [labels (2) and (4)] were attributed to the different polytypes.

Label (5) in the Figure 1.6 shows the exciton energy calculated from the deconvoluted imaginary part of the dielectric function, which was obtained by ellipsometric measurements [58] of $TlInS_2$ in ***E*//*c****. Clearly, in the C phase, a rapid energy shift is observed with decreasing temperature; however, the energy values are smaller than those obtained by PL measurements. The authors attributed this energy difference to the different configurations used in the experiments, ***E*//*c**** in [58] while and ***E*⊥*c**(*k*//*c**)** in [55–56]

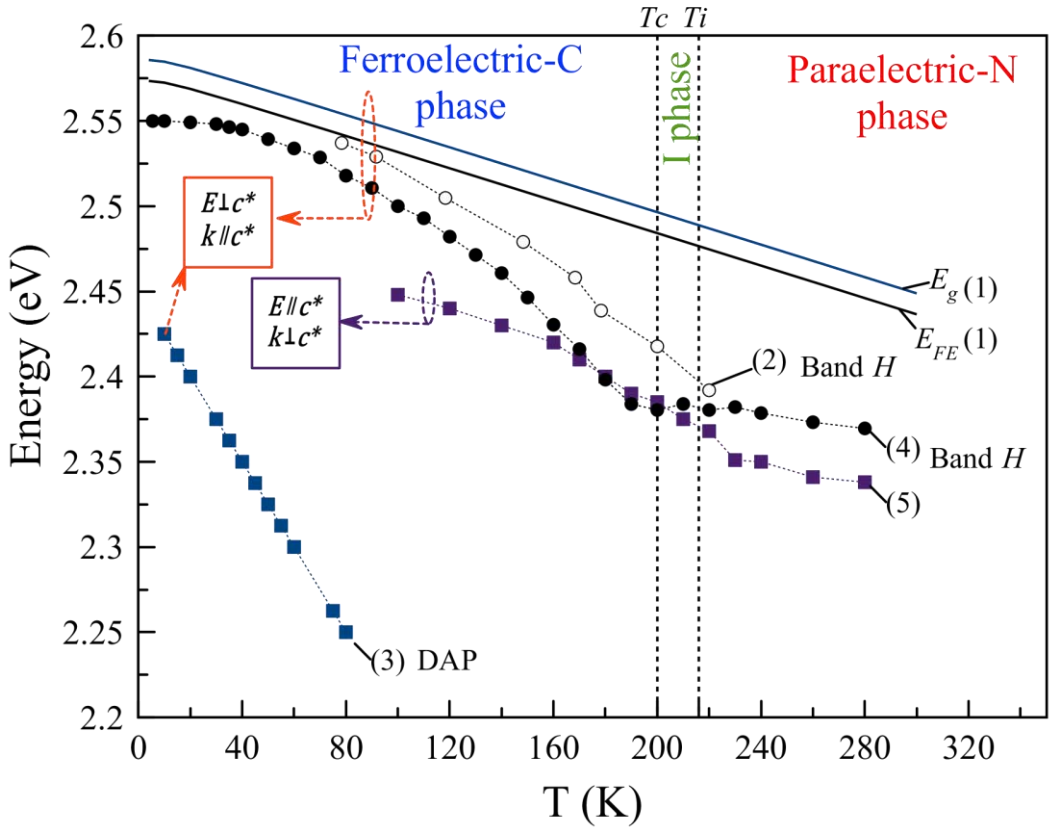

Figure 1.6 The results of early studies near the fundamental band edge by transmissions, reflections, ellipsometry, and photoluminescence (PL) measurements in $TlInS_2$.

To our knowledge, the existence of excitonic emission near the fundamental band edge of the PL spectra of $TlGaSe_2$ remains unconfirmed and has so far received little attention.

1.3.2 Raman scattering studies of $TlInS_2$ and $TlGaSe_2$

Early studies on the polarized Raman scattering of $TlInS_2$ and $TlGaSe_2$ at 300 K have been reported [5, 59–62]. However, at the time of those studies, the structure of these layered crystals was considered to be tetragonal, as shown in Figure 1.7. Therefore, the assignations of the optical modes characterizations were performed according to the tetragonal structure, D_{4h}. Actually, we know the existence of several polytypes, i.e. layered crystals with monoclinic structure.

Polarized Raman spectra
of $TlInS_2$ and $TlGaSe_2$ **crystal at 300 K**[1]

symmetry		crystal $TlGaSe_2$		$TlGaS_2$	$TlInS_2$
C_{4h}	D_{4h}	300 K	4.2 K	300 K	300 K
A_g	A_{1g}	41.5	47	44.5	43
		92	126	124	100
		133.5	187	186	138
			315.5	311.5	282.5
		194.5	320.5	316.5	294
		194.5	329	324	
		270	355	350	301
B_g	B_{1g}	40.5		45.5	39
		46		53	50
		53.5	72.5	68	57
				151	
		279.5		390	347
	B_{2g}		78.5	76	
		80	115.5	111.5	81
E_g	E_g	19	22	22.5	18.5
				29	24.5
		31.5	41	42.5	34.5
		83	122	121	89.5
		105	174	175	128.5
		231.5	335	326	304
			348.5	345.5	

Figure 1.6 Early studies of polarized Raman scattering of $TlInS_2$ and $TlGaSe_2$ [5].

Additionally, the temperature dependence of the unpolarized Raman scattering has been investigated in [25–27]. However, these studies did not consider the existence of structural phase transitions; therefore, the behaviors of the Raman lines positions and widths were explained through thermal expansion and the anharmonicity theory.

1.4 Study purpose

The aim of this work was to study the relationship between the optical properties of layered ternary thallium chalcogenide crystals and their structural phase transitions. In this work, the band-edge region of the PL spectra of monoclinic $TlInS_2$ and $TlGaSe_2$ crystals were measured using a confocal microscopy system and investigated in terms of the excitation density dependence at 77 K and over the temperature range 77–300 K, which includes the region of successive phase transitions. Furthermore, we will discuss the temperature dependence of the Raman spectra in single-crystal $TlInS_2$ and $TlGaSe_2$ obtained in the low-frequency region, down to 35 cm^{-1}. It is commonly believed that the phase transitions in $TlInS_2$ and $TlGaSe_2$ are connected with the displacement of Tl^+ atoms. Because these atoms are very heavy, the low-frequency region of the Raman spectra of these compounds is of particular interest.

References

[1] D. Müller, G. Eulenberger, and H. Hahn, Z. Anorg. Allg. Chem., vol. 398, pp. 207–220 (1973).

[2] D. Müller and H. Hahn, Z. Anorg. Allg. Chem., vol. 438, pp. 258–272 (1978).

[3] N. M. Gasanly, A. F Goncharov, B. M. Dzhavadov, N. N. Melnik, V. I. Tagirov, and E.A. Vinogradov, Phys. Stat. Sol. B, vol. 97, pp. 367–377 (1980).

[4] W. Henkel, H.D. Hochheimer, C. Carlone, A. Werner, S. Ves, and H. G.V. Schnering, Phys. Rev. B, vol. 26, pp. 3211–3221 (1982).

[5] N. M. Gasanly, A. F Goncharov, N. N. Melnik, A. S. Raginov, and V. I. Tagirov, Phys. Stat. Sol. B, vol. 116, pp. 427–443 (1983).

[6] K. A. Yee and A. Albright, J. Am. Chem. Soc., vol. 113, p. 6474 (1991).

[7] S. Kashida and Y. Kobayashi, J. Phys.: Condens. Matter 11, pp. 1027–1035 (1999).

[8] G. E. Delgado et al., Physica B 391, pp. 385–388 (2007).

[9] G. E. Delgado et al., Crys. Res. Technol. 42, No. 7, pp. 663–666 (2007).

[10] G. D Guseinov et al., Phys. Stat. Sol. vol. 34, pp. 33–44 (1969).

[11] M. Hanias, A. Anagnostopoulos, K. Kambas, and J. Spyridelis, Physica B, vol. 160, pp. 154–160 (1989).

[12] M. Hanias, A. Anagnostopoulos, K. Kambas, and J. Spyridelis, Mat. Res. Bull., vol. 27, pp. 25–38 (1992).

[13] H. Uchiki, D. Kanazawa, N. Mamedov, and S. Iıda, J. Lumin., vol. 87–89, pp. 664–666 (2000).

[14] S. Ozdemir et al., Solid State Comm., vol. 96, pp. 821–826 (1995).

[15] N. Mamedov et al., Thin Solid Films 49, pp. 275–278 (2006).

[16] I. M. Ashraf, M. M. Abdel-Rahman, and A. M. Badr, J. Phys. D, vol. 36, p. 109 (2003).

[17] N. Kalkan, D. Papadopoulos, A. N. Anagnostopoulos, and J. Spyridelis, Mat. Res. Bull., vol. 28, pp. 693–707 (1993).

[18] F. Qasrawi and N. M. Gasanly, Phys. Status Solidi A, vol. 199, p. 277 (2003).

[19] Y. Shim, N. Uneme, S. Abdullayeva, N. Mamedov, and N. Yamamoto, J. Phys. Chem. Solids, vol. 66, pp. 2116–2118 (2005).

[20] A. M. Panich, J. Phys.: Condens. Matter, vol. 293202 (2008).

[21] M. M. El-Nahass, M. M. Sallam, and A. H. S. Abd Al-Wahab, Curr. Appl. Phys., vol. (2009).

[22] A. M. Panich, R. M. Sardarly, Physical properties of the low-dimensional A3B6 and $A^3B^3C^6_2$ compounds, Nova, (2010).

[23] S. Johnsen et al., Chem. Mater., vol. 23, pp. 3120–3128 (2011).

[24] A. Owens, Compound Semiconductor Radiation Detectors, CRC Press, (2012).

[25] N. S. Yuksek, N. M. Gasanly, and A. Aydinli, J. Raman Spectroscopy, vol. 35, p.55 (2004).

[26] N. S. Yuksek, N. M. Gasanly, and H. Ozkan, J. Korean Phys. Soc., vol. 45, p. 501 (2004).

[27] N. S. Yuksek and N. M. Gasanly, Cryst. Res. Technol., vol. 40, pp. 264-270 (2005).

[28] A. A. Volkov, Y. G. Goncharov, G. V. Kozlov, K. R. Allakhverdiev, and R. M. Sardarly, Sov. Phys. Solid State 25, pp. 2061–2062 (1983).

[29] A. A. Volkov, Y. G. Goncharov, G. V. Kozlov, S. P. Lebedev, A. M. Prokhorov, R. A. Aliev, and K. R. Allakhverdiev, JETP Lett., vol. 37, p. 615 (1983).

[30] R. A. Aliev, K. R. Allakhverdiev, A. I. Baranov, N. R. Ivanov, and R. M. Sardarly, Sov. Phys. Solid State 26, pp. 775–778 (1984).

[31] S. B. Vakhrushev, V. V. Zhdanova, B. E. Kvyatkovsky, V. N. Okuneva, K. R. Allakhverdiev, R. A. Aliev, and R. M. Sardarly, JETP Lett., vol. 39, p. 291 (1984).

[32] A. A. Volkov, Y. G. Goncharov, G. V. Kozlov, and R. M. Sardarly, Sov. Phys. Solid State 39, p. 351 (1984).

[33] V. M. Burlakov, S. Norov, and A. P. Ryabov, Sov. Phys. Solid State 30, pp. 2077–2079 (1988).

[34] H. D. Hochheimer et al., Z. Phys. B, Condens. Matter 73, pp. 257–263 (1988).

[35] D. F. McMorrow et al., J. Phys. Condens. Matter 2, pp. 3699–3712 (1990).

[36] F. M. Salaev, K.R. Allakhverdiev, and F. A. Mikailov, Ferroelectrics, vol. 131, pp. 163–167 (1992).

[37] K.R. Allakhverdiev, F. M. Salaev, F. A. Mikailov, and T. S. Mamedov, JETP Lett., vol. 56, p.149 (1992).

[38] K.R. Allakhverdiev, N. Türetken, F. M. Salaev, and F. A. Mikailov, Solid State Comm., vol. 96, p. 827 (1995).

[39] K.R. Allakhverdiev, S. Ellialtioglu, and N, M. Gasanly, Solid State Comm., vol. 88, pp. 387–390 (1993).

[40] K. K. Mamedov, A. M. Abdullaev, and E. M. Kerimova, Phys. Status Solidi A, vol. 94, pp. 115–119 (1986).

[41] B. R. Gadjiev, N. T. Mamedov, and F. B. Godjaev, Sov. Low Temp. Phys., vol. 20, p. 7448 (1994).

[42] N. A. Abdullaev, K. R Allakhverdiev, G. L Belenkii, T. G Mamedov, R. A. Suleimanov and Y. N. Sharifov, Solid State Comm., vol. 53, pp. 601–602 (1985).

[43] T. G. Mamedov and R. A. Suleymanov, Physics of the Solid State, vol. 45, pp. 2242–2248 (2003).

[44] K. R. Allakhverdiev, T. G. Mammadov, R. A. Suleymanov, and N. Z. Gasanov, Condens. Matter 15, pp. 1291–1298 (2003).

[45] A. E. Bakhyshov et al., Phys. Status Solidi B, vol. 95, K121 (1979).

[46] A. E. Bakhyshov et al., Sov. Phys. Semicond. 12, pp. 320 (1978).

[47] R. M. Sardarly et al. Physics of the Solid State, vol. 47, pp. 1729–1733 (2005).

[48] V. Grivickas et al., Phys. Status Solidi B, vol. 244, 4624–4628 (2007).

[49] O. Z. Alekperov and A. I. Nadjafov, Inorg. Mater, vol. 40, pp. 1248–1251 (2004).

[50] O. Z. Alekperov and A. I. Nadzhafov, Inorg. Mater, vol. 45, pp. 7–12 (2009).

[51] N. A. Borovoi et al., Physics of the Solid State, vol. 51, pp. 2367–2370 (2009).

[52] N. A. Borovoi et al., Inorg. Mater, vol. 45, pp. 1–6 (2009).

[53] J. A. Kalomiros and A. Anagnostopoulos, Phys. Rev. B, vol. 50, pp. 7488–7494 (1994).

[54] P. Lautenschlager, M. Garriga, S. Logothetidis, and M. Cardona, Phys. Rev. B, vol. 35, pp. 9174–9189 (1987).

[55] K. R. Allakhverdiev, M. N. Gasanly, and A. Aydinli, Solid State Comm., vol. 94, pp. 777–782 (1995).

[56] T. Arai et al., Ternary and Multinary Compounds in the 21st Century, IPAP Books 1, pp. 24–32 (2001).

[57] A. Aydinli, N. N. Gasanly, I Yilmaz, and A. Serpenguzel, Semicond. Sci. Technol. 14, pp. 599–603 (1999).

[58] N. Mamedov, Y. Shim, W. Okada, R. Tashiro, and K. Wakita, Phys. Stat. Sol. B, vol. 252, pp. 1248–1253 (2015).

[59] T. J. Isaac and J. D. Feichtner, J. Solid. State. Chem., vol. 14, p. 260 (1975).

[60] E. A. Vinogradov, G. N. Zhizhin, N. N. Melnik, S. I. Subbotin, V. V. Panfilov, K. R. Allakhverdiev, E. Yu. Salaev, and R. Kh. Nani, Phys. Status B 95, p. 383 (1979).

[61] R. Sardarly, F. Wondre, I. F. Ryan, and K. Allakhverdiev, Phys. Stat. Sol. B, vol. 88, p. K5 (1978).

[62] B. N. Marvrin, Kh. E. Sterin, N. M. Gasanly, Z. D. Khalafov, E. Yu. Salaev, K. R. Allakhverdiev, and R. M. Sardarly, Fiz. Tverd. Tela (Leningrad) 19, p. 2960 (1977).

CHAPTER 2

Theoretical Background

2.1 Introduction

This chapter briefly introduces the concepts underlying PL and Raman scattering.

2.2 Photoluminescence

Atoms spontaneously emit light when electrons in an excited state move to a lower state (ground state) by radiative transition. In solids, the radiative emission process is called luminescence, and can occur throught a number of mechanisms [1–5]:

- Electroluminescence: Light emission resulting from exciting the sample by the injection of electrons and holes via an external current.
- Thermoluminescence: Light emission caused by heating the sample.
- Cathodoluminescence: Light emission induced by electron bombardment.
- Photoluminescence: The re-emission of light after absorbing a photon of energy greater than the bandgap energy.

In this work, we only consider photoluminescence.

Absorption and emission are related to each other. In the absorption process, energy is removed from an incident electromagnetic wave while electron–hole pairs are created. Emission is the reverse of this process, i.e., an electron–hole excited in the medium is destroyed, resulting in the emission of electromagnetic radiation; the electron–hole pairs are said to have undergone radiative recombination [3]. Moreover, radiative emission is not the only mechanism. An alternative pathway between the excited-state and ground-state bands is non radiative relaxation. Here, the electron might lose its excitation energy as heat by emitting phonons or it may transfer this energy to impurities. In the following, we consider in more detail the various radiative recombination processes commonly observed in semiconductors, shown in Figure 2.1

[3]. Unless otherwise specified, we assume that the electron–hole pairs have been excited optically, i.e., the experimental technique is photoluminescence.

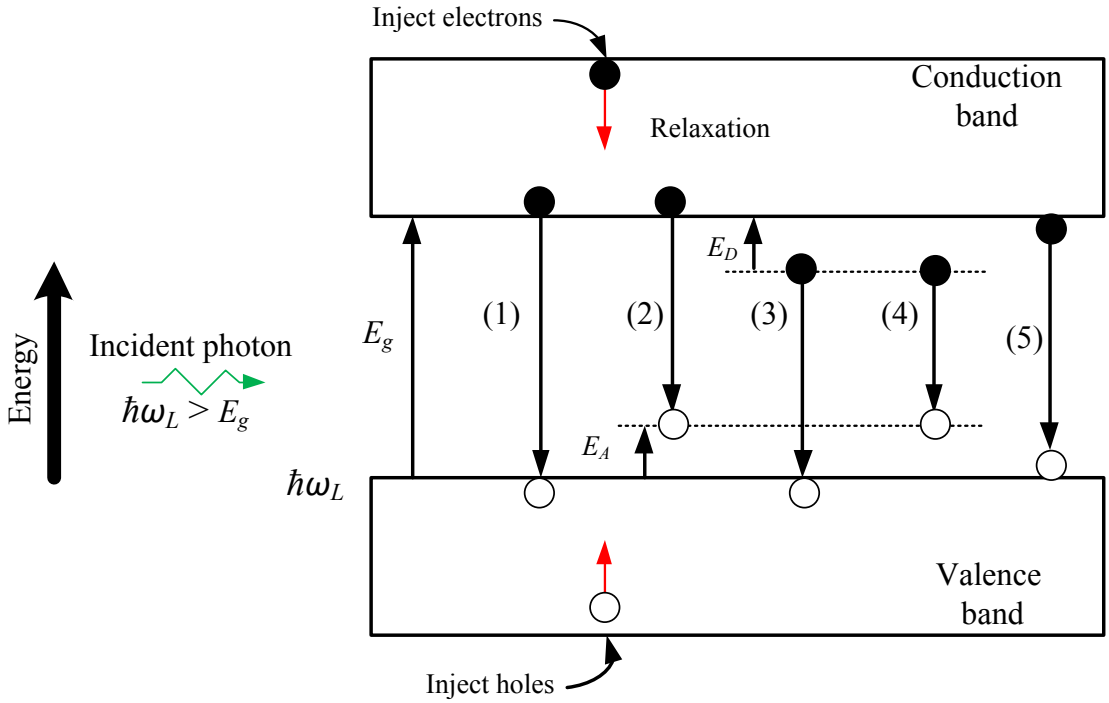

Figure 2.1 Radiative recombination processes commonly observed in semiconductors: (1) Band-to-band transition, (2) free-electron-to-neutral-acceptor transition, (3) free-hole-to-neutral-donor transition, (4) DAP reconbination, and (5) excitonic recombination. E_g is the bandgap energy and E_A and E_D are the shallow acceptor and donor binding energy, respectively.

2.2.1 Band-to-band transition

In a perfect semiconductor, electron–hole pairs thermalize and accumulate at the conduction and valence band extremes, where they tend to recombine. If this semiconductor has a direct bandgap and electric dipole transitions are allowed, the electron–hole pairs will recombine radiatively with a high probability. In indirect-band semiconductors, electron–hole pairs can recombine radiatively only via phonon-assisted transitions. Band-to-band transitions tend to dominate at higher temperatures where all the shallow impurities are ionized.

2.2.2 Free-electron-to-neutral-acceptor transition

At sufficiently low temperatures, carriers are trapped in impurities. For example, consider a PL experiment on a p-type sample containing N_A acceptors per unit volume. At low photoexcitation density, the density n_e of the free electrons created in the conduction band is much smaller than N_A. These free electrons can recombine radiatively (sometimes also non-radiatively) with the holes trapped in the acceptors. Such transitions, which involve a free carrier (in this case, an electron) and a charge (a hole) bound to an impurity are known as free-electron-to-neutral-acceptor transitions. The emitted photon energy in this sample is given by $E_g - E_A$, where E_g and E_A are the bandgap energy and the shallow acceptor binding energy, respectively. A similar explanation could be used in free-hole-to-neutral-donor transition.

2.2.4 Donor−acceptor pair recombination

Often a semiconductor contains donors and acceptors. Such semiconductors are called compensated because, under equilibrium conditions, some of the electrons from the donor are captured (or compensated) by the acceptors. As a result, a compensated sample contains both ionized donors (D^+) and acceptors (A^-). By optical excitation, electron and holes can be created in the conduction and valence bands, respectively. These carriers can then be trapped at the D^+ and A^- sites to produce neutral D^0 and A^0 centers. When returning to equilibrium, some of the electrons of the neutral donors will recombine radiatively with holes of the neutral acceptors. This process is known as a DAP recombination.

2.2.5 Excitons and bound excitons

The absorption of a photon by an interband transition in a semiconductor creates an electron in the conduction band and a hole in the valence band at the same point in space, that can attract each other through their mutual Coulomb interaction. If the appropriate conditions are satisfied, a neutral bound electron–hole pair can be formed, which is called an exciton.

The free exciton (FE) emission process is simply the radiative decay of excitons into phonons. Because the wave vector must be conserved in this process, only excitons with wave vectors equal to the photon wave vector can be converted to photons. When

these FEs lose their kinetic energy owing to localization at the lattice defects (traps), they are called bound excitons.

2.2 Raman scattering

The term Raman scattering is historically associated with the scattering of light by optical phonons in solid and molecular vibrations [6]. Here, the term refers to inelastic scattering durin which a light beam is scattered by an optical medium and changes its frequency in the process. This is in contrast to elastic light scattering, in which the frequency of the light is unchanged (Rayleigh scattering).

Inelastic scattering processes are two-photon events that involve the simultaneous annihilation of an incident photon and the creation of a scattered photon [6]. The interaction process and the transition schemes are illustrated in Figure 2.2 and Figure 2.3, respectively. An incident photon (monochromatic light beam) with an angular frequency ω_L and a wave vector $\boldsymbol{k_L}$ is scattered by exciting a medium of frequency ω_q and wave vector $\boldsymbol{q}$. The scattered photon has a frequency ω_S and a wave vector $\boldsymbol{k_S}$. The excitation of the medium may be manifested in many different types of elementary excitations that occur in a crystal, such as phonons, magnons, or plasmons. Here, we are concerned exclusively with the phonon process.

Inelastic light scattering from phonons can be divided into two generic types [6]:

- Stokes scattering
- Anti-Stokes scattering

If the frequency of the scattered photon, $\boldsymbol{\omega_S}$, is smaller than that of the incident photon, $\boldsymbol{\omega_L}$, a quantum of energy, $\hbar(\omega_L - \omega_S)$, is added to the scattering medium and the event is referred to as a Stokes process. In contrast, if, $\boldsymbol{\omega_L} < \boldsymbol{\omega_S}$ we have an anti-Stokes process, where the elementary excitation of the medium is eliminated. In this case, the conservation of energy and momentum during the interaction requires that

$$\boldsymbol{k_S} = \boldsymbol{k_L} \pm \boldsymbol{q} \qquad (2.1)$$

$$\omega_S = \omega_L + \omega_S \qquad (2.2)$$

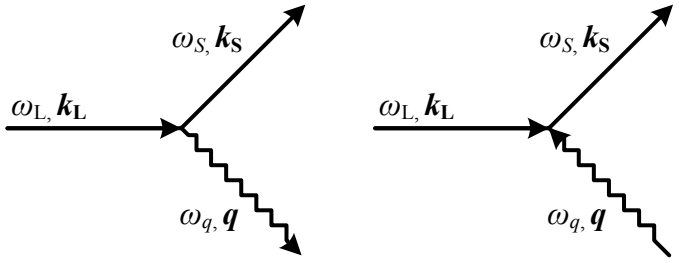

(a) (b)

Figure 2.2 Interactions in inelastic (a) Stokes and (b) anti-Stokes light scattering. The straight arrows represent photons, whereas the wavy arrows represent phonons.

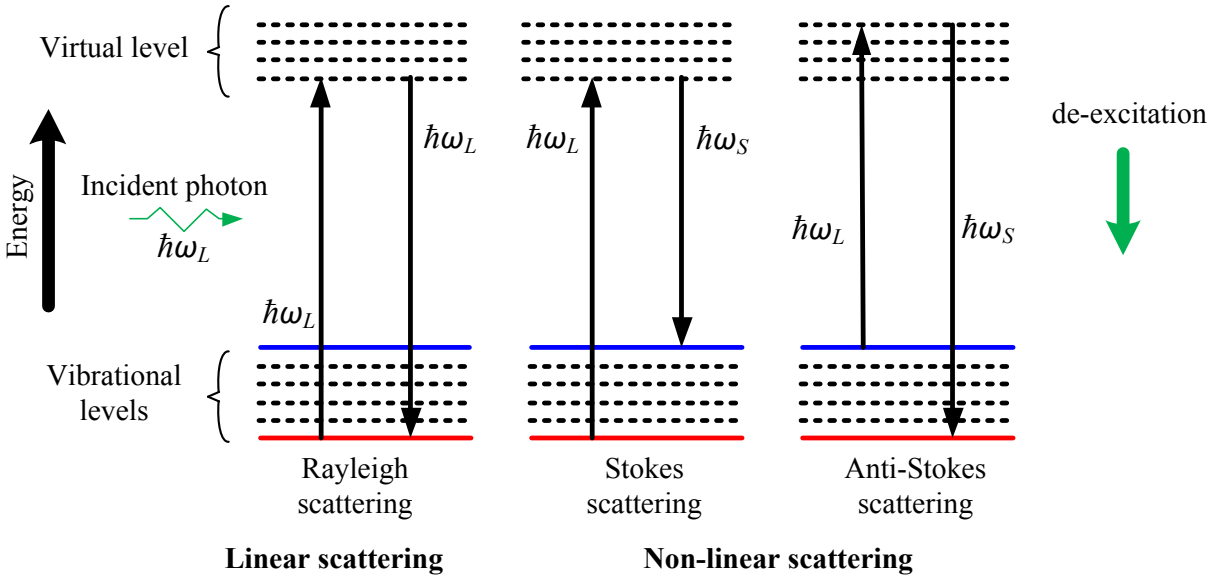

Figure 2.3 Transition scheme of inelastic light scattering.

The plus signs (+) in Equations 2.1 and 2.2 correspond to Stokes scattering (photon emission), whereas the minus sign (–) corresponds to anti-Stokes scattering (phonons absorption). Moreover, we can see in Figure 2.3 that anti-Stokes scattering is only possible if there are phonons present in the material before the application of the incident light. Therefore, the probability of anti-Stokes scattering decreases with decreasing temperature because the phonon population decreases.

References

[1] I. Pelant and J. Valenta, Luminescence Spectroscopy of Semiconductors, Oxford University Press, (2012).

[2] M. Fox, Optical Properties of Solids, Oxford, 2nd ed., (2010).

[3] P. Y. Yu and M. I. Cardona, Physics and Materials Properties, Springer, (1996).

[4] C. F. Klingshirn, Semiconductor Optics, Springer-Verlag, Berlin, (1997).

[5] J. I. Pankove, Optical Processes in Semiconductors, Prentice-Hall, (1971).

[6] W. H. Weber and R. Merlin (Eds.), Raman Scattering in Materials Sciences: Springer Series in Materials Science, (2000).

CHAPTER 3

Experimental setup

3.1 Introduction

In this work, Raman scattering and PL spectroscopy were performed using a confocal spectroscopy system. In this sub-section, we will present a brief description of the system and the operation of the confocal microscope. Moreover, we focus on the $TlInS_2$ and $TlGaSe_2$ crystals and the polarizations geometries used in the measurements.

3.2 Confocal spectroscopy system

A schematic diagram of a confocal spectroscopy system (extended Nanofinder 30, Tokyo Instruments [1]) is shown in Figure 3.1b. In our system, we used two excitation sources: a diode-pumped solid-state (DPSS) Nd: yttrium-aluminium-garnet (YAG) laser operating at 532 nm and a femtosecond pulsed Ti: sapphire laser (Mai Tai VF-TIS, Spectra Physics) at 750 to 850 nm (tunability of 1 nm). The Ti: sapphire laser was also used as a fundamental wave to obtain the second harmonic generation (SHG) (GWU23F, Spectra Physics). The laser beam power could be attenuated with the help of a circular variable metallic neutral density (ND) filter.

The Raman scattering and PL spectroscopy are performed using a charge-coupled device (CCD) (DV420A-OE, Tokyo Instruments) as a detector. The configuration of the system parameters for each measurement (Raman scattering or PL) was performed with a computer. The system was also capable of performing time-resolved PL and laser reflection intensity mapping measurements using a streak camera and a photomultiplier-tube (PMT), respectively. As these components were not used in this work, no further information is provided. The continuous-flow cryostat (ST-500, JANIS) stage allowed the performance of materials characterization at various temperatures.

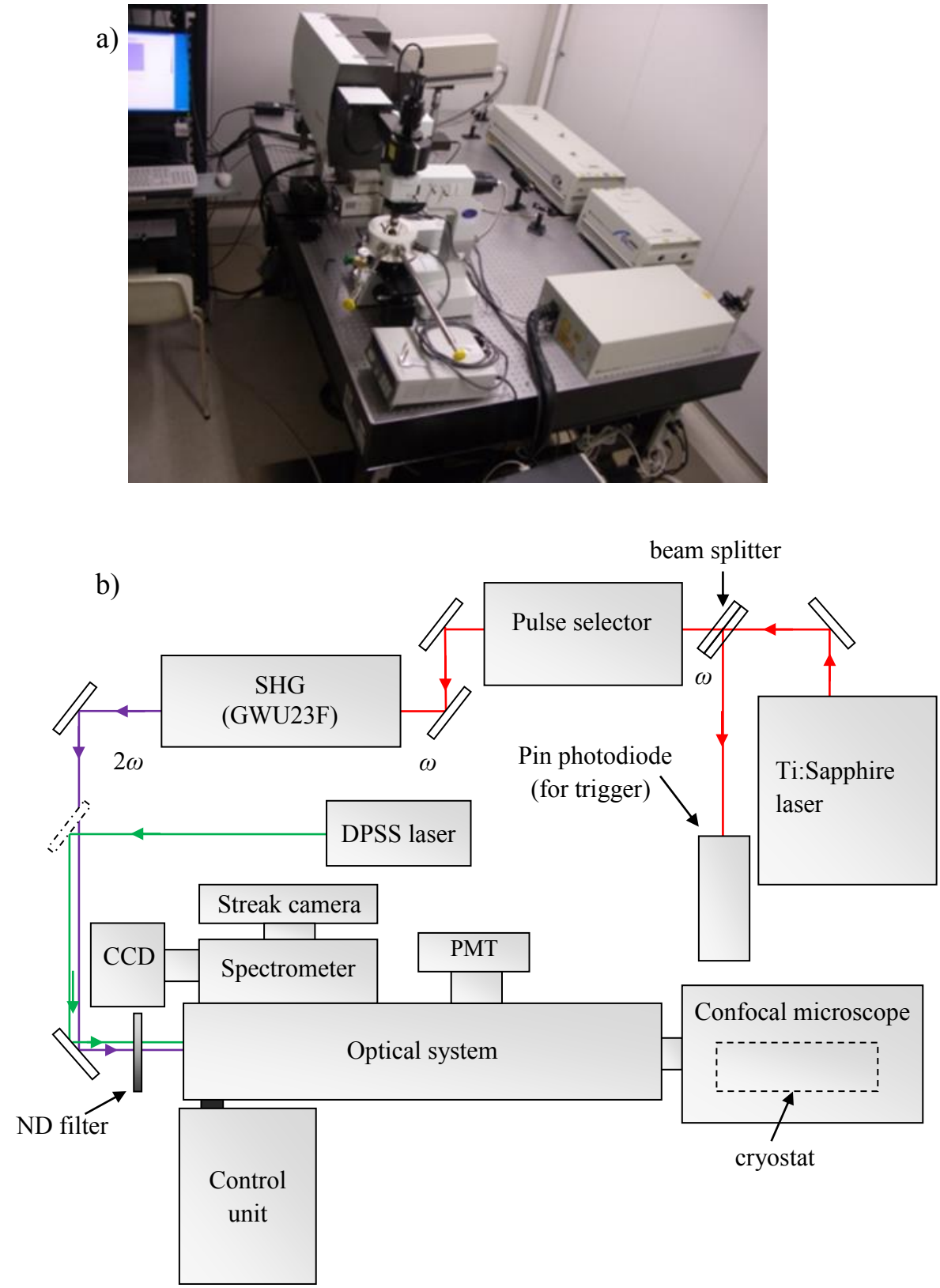

Figure 3.1 a) Extended Nanofinder 3, Tokyo Instrument. b) Schematic diagram of confocal spectroscopy system.

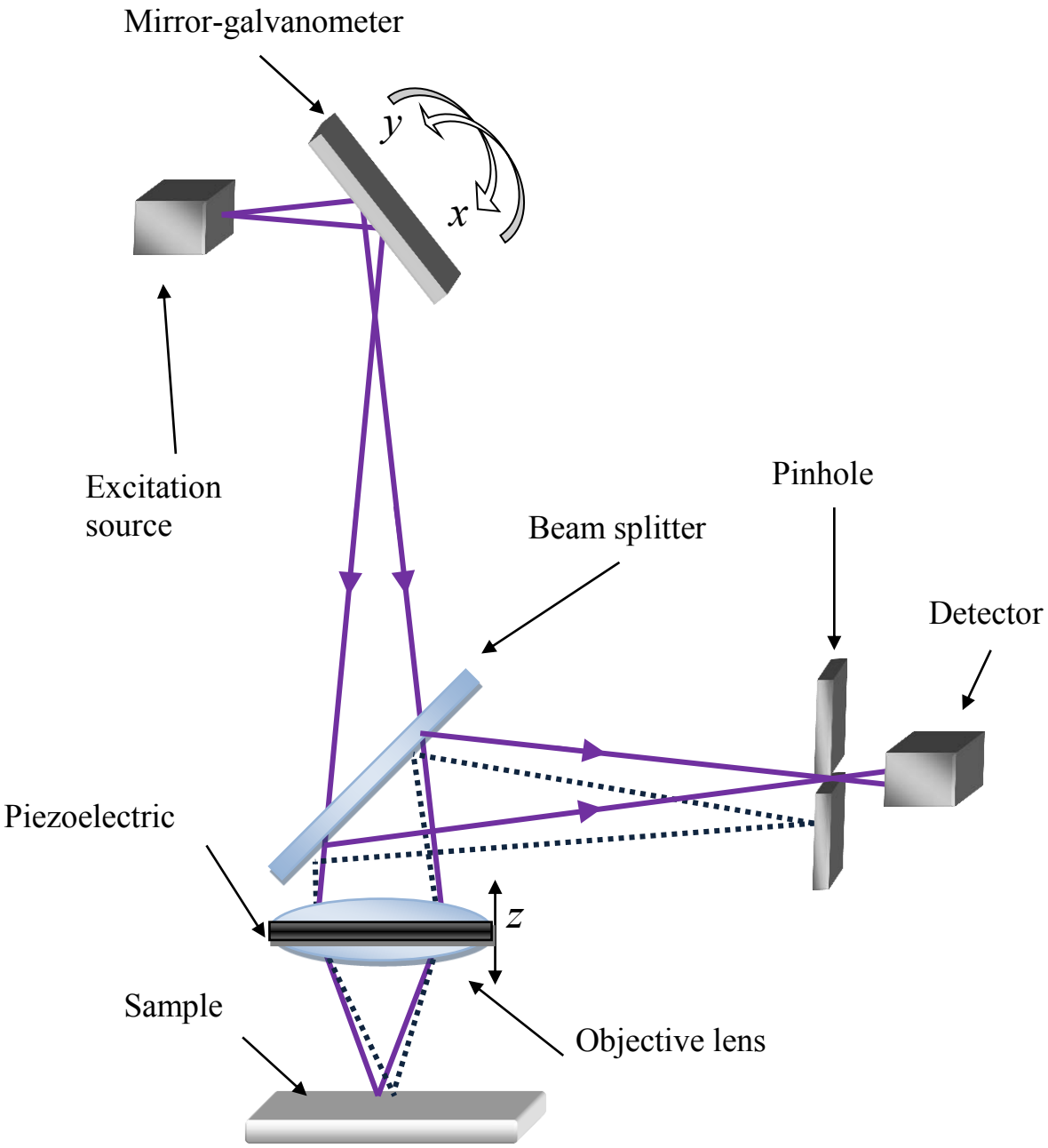

Figure 3.2 Basic setup of a confocal microscope

3.2.1 Confocal microscope operation

The basic setup of a confocal microscope is shown in Figure 3.2. In confocal microscopy, a point-like source is focused onto the sample using an objective lens. Directional alignment in the *x* and *y* directions can be performed by a mirror mounted on a galvanometer motor for focus control, whereas the *z* direction is adjusted by a piezoelectric device mounted on the objective. The scattered light and the reflected laser beam return on the same path through the objective lens and are separated by a beam splitter, where the scattered light is redirected to the detector through a pinhole that allows only light from the focal plane to reach the detector. Thus, image contrast is enhanced. Moreover, by choosing an appropriate pinhole diameter, the lateral resolution can be increased by up to a factor of 1.41. A two-dimensional image of the sample surface can be obtained by scanning the sample with respect to the objective.

3.3 Photoluminescence spectroscopy experimental setup

Figure 3.3a shows a schematic diagram of our PL measurement system. The sample was mounted in a continuous-flow cryostat. A pulsed laser source Ti:sapphire laser and an SHG were used as excitation sources with wavelengths of 800 and 400 nm (3.3 eV), respectively. The typical laser spot size on the crystal surface was approximately 25–200 μm. The obtained excitation densities were in the range 0.01–1 MW/cm^2. The PL was measured using a confocal microspectroscopy system and a CCD detector. The measurements were conducted at temperatures ranging from 77 to 300 K.

3.4 Raman spectroscopy experimental setup

Figure 3.3b shows a schematic diagram of our Raman scattering measurement system. A DPSS Nd:YAG laser with a wavelength of 532 nm was used as the light source for the Raman confocal microscope system. The spectral resolution of the system was better than 0.8 cm^{-1}. The temperature of the sample, which was placed in a special vibration-free cryostat, varied from 77 to 300 K, covering successive phase transitions of the $TlInS_2$ and $TlGaSe_2$ compounds.

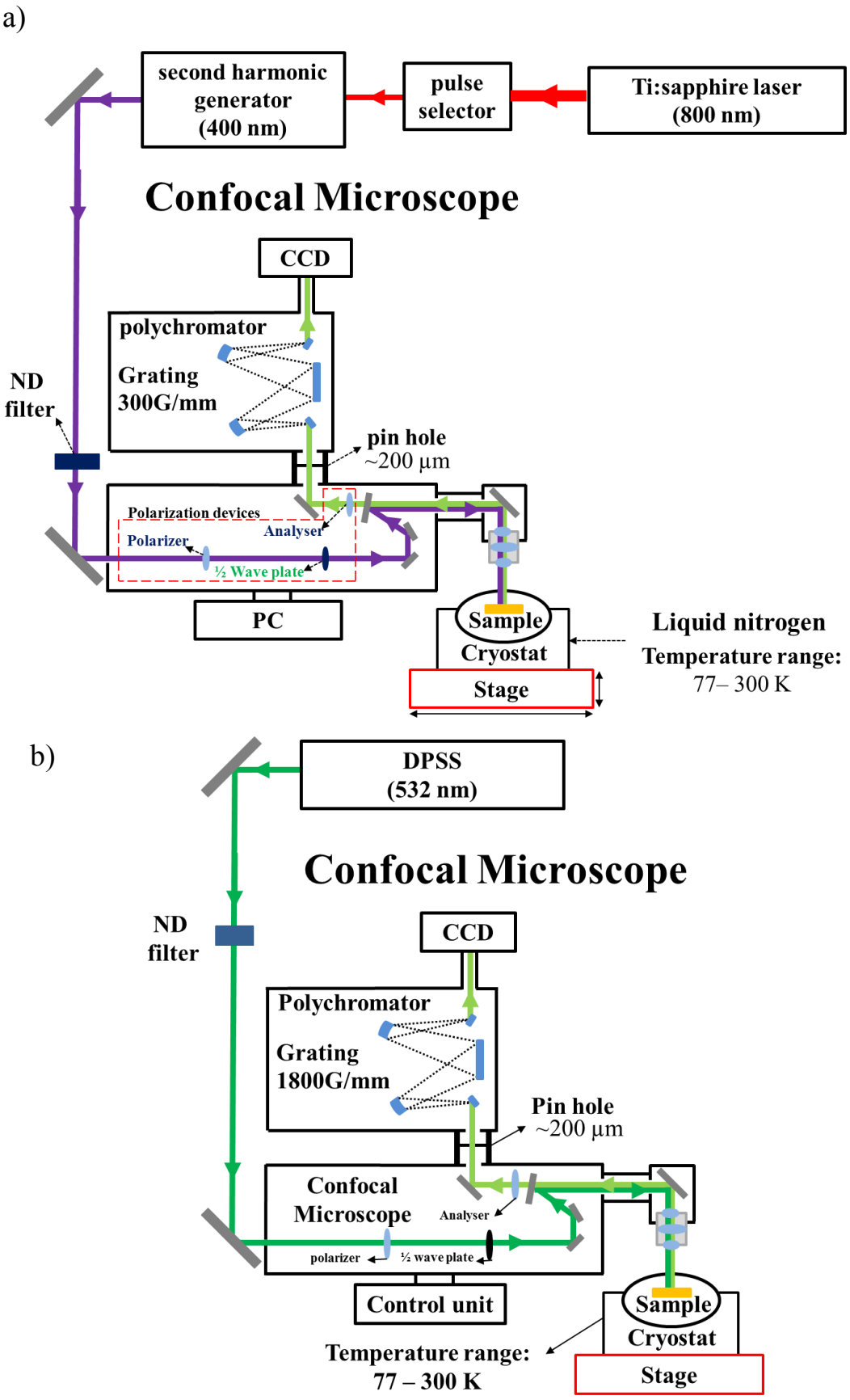

Figure 3.3 Schematic diagram of our PL (a) and Raman scattering (b) measurement system.

3.5 $TlInS_2$ and $TlGaSe_2$ crystals

Single crystals of layered $TlInS_2$ and $TlGaSe_2$ were grown by using the Bridgman−Stockbarger method [2]. The obtained crystals could be easily cleaved into plane-parallel plates perpendicular to the crystallographic ***c**** axis. The XRD patterns showed that the polytype of the studied crystals were C-$TlInS_2$ and C-$TlGaSe_2$, with parameter $\boldsymbol{c} \approx 15$Å of the monoclinic system in the space group $C2/c$ [3–6]. Figures 3.4 show the crystals studies in this work.

3.6 Polarizations geometries

The PL and Raman scattering spectra were measured in the backscattering configuration in two geometries, as shown in the Figure 3.5: (1) On the surface of the crystal parallelly to the ***ab*** plane, (001) plane, where the propagation vectors of the incident light ($\boldsymbol{k}_i$) and the PL emission ($\boldsymbol{k}_e$) or scattering ($\boldsymbol{k}_s$) are parallel to the ***c*** axis, as shown in Figure 3.5a and 3.5c, respectively. Note that in this configuration, the electrical vector (***E***) of the incident and emission light are perpendicular to the ***c*** axis ($\boldsymbol{E} \perp \boldsymbol{c}^*$). And (2) on the surface of the crystal that is perpendicular to the (001) plane where the propagation vectors of the incident light ($\boldsymbol{k}_i$) and the PL emission ($\boldsymbol{k}_e$) or scattering ($\boldsymbol{k}_s$) are perpendicular to the ***c*** axis, as shown in Figure 3.5b and 3.5d, respectively.

In polarized Raman scattering, according to Porto's notation, the examined polarization geometry showed in the Figure 3.5d was $x(zz)\bar{x}$, where x and $\bar{x}$ represent the propagation directions of the incident ($\boldsymbol{k}_i$) and scattered ($\boldsymbol{k}_s$) light, respectively, whereas the first and second letters inside the parentheses denote to the polarization of the incident ($\boldsymbol{E_i}$) and scattered radiation ($\boldsymbol{E_s}$), respectively. In the case of the polarization $x(yy)\bar{x}$, the propagation directions of the incident ($\boldsymbol{k}_i$) and scattered ($\boldsymbol{k}_s$) light are papallelly to the ***x*** axis, whereas the polarization of the incident ($\boldsymbol{E_i}$) and scattered radiation ($\boldsymbol{E_s}$) are parallelly to the y axis.

a)

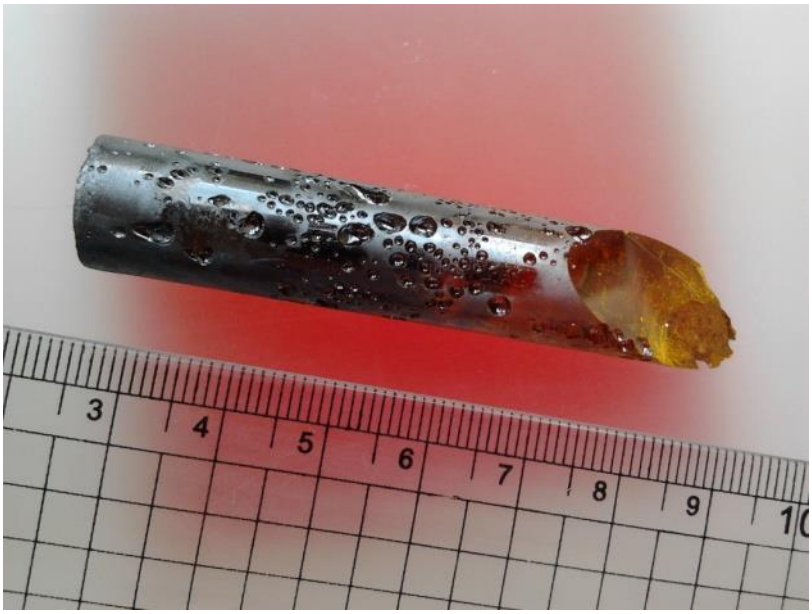

b)

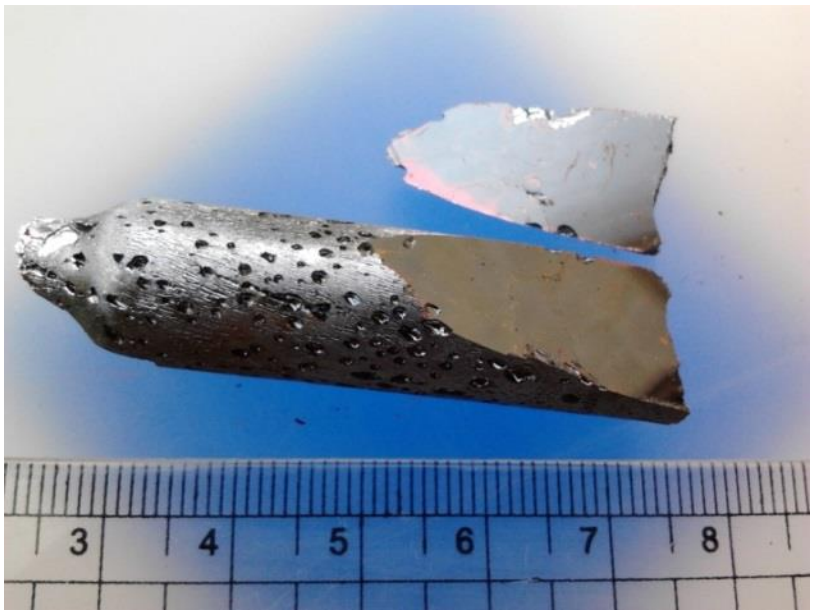

Figure 3.4 Crystals studies in this work, C-$TlInS_2$(a) and C-$TlGaSe_2$ (b)

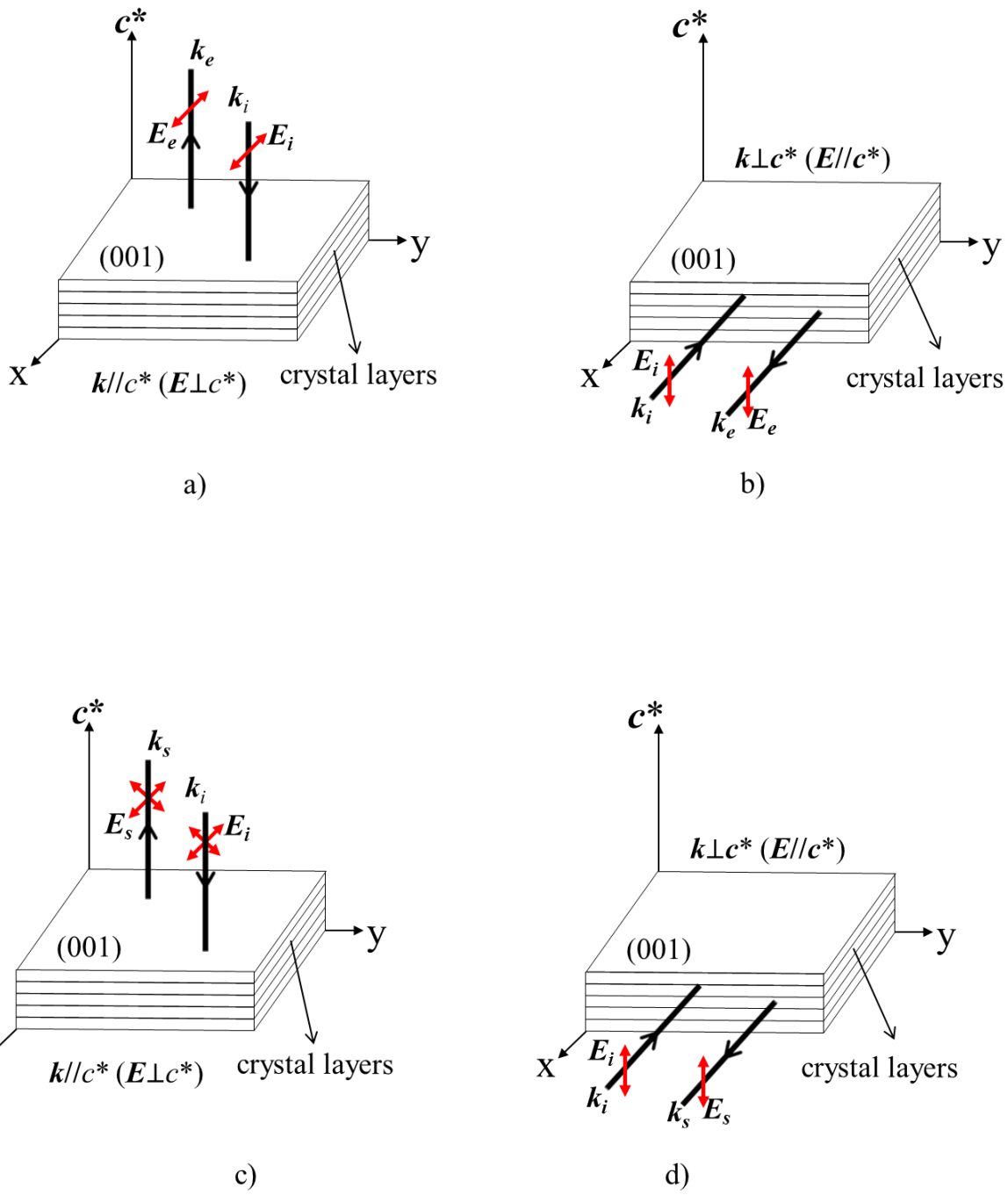

Figure 3.5 Key diagram of the PL and Raman scattering measurement set up in backscattering configuration. The direction of the excitation light (k_e) is perpendicular to the plates of the crystal *a and c). The direction of the excitation light (k_e) is parallel to the plates of the crysta (b and d).

3.7 Summary

In this chapter, we have provided a description of the confocal spectroscopy system and the basic principle behind the operation of the confocal microscope, and discussed some experimental considerations regarding to the polarization geometry used in the measurements.

References

[1] http://www.tokyoinst.co.jp/

[2] O. Z. Alekperov and A. I. Nadjafov, and T. G. Mamedov, Azerbaifzhan Patent a 2005 02 78.

[3] O. Z. Alekperov and A. I. Nadjafov, Inorg. Mater, vol. 40, pp. 1248–1251 (2004).

[4] O. Z. Alekperov and A. I. Nadzhafov, Inorg. Mater, vol. 45, pp. 7–12 (2009).

[5] N. A. Borovoi et al., Physics of the Solid State, vol. 51, pp. 2367–2370 (2009).

[6] N. A. Borovoi et al., Inorg. Mater, vol. 45, pp. 1–6 (2009).

CHAPTER 4

Photoluminescence spectroscopy of $TlInS_2$ and $TlGaSe_2$

4.1 Introduction

This chapter describes the PL spectra of quasi-two-dimensional ternary thallium dichalcogenide $TlInS_2$ and $TlGaSe_2$ using a confocal microscope system in the temperature range from 77 to 300 K, in which a series of phase transitions is believed to occur. The PL spectra and their excitation intensities and temperature dependences are then used to propose a model for the recombination process of photo-excited carriers.

4.2 PL spectra of $TlInS_2$

Figure 4.1 shows the PL spectra of $TlInS_2$ for light polarization $\boldsymbol{E}\perp\boldsymbol{c}^*(\boldsymbol{k}//\boldsymbol{c}^*)$ and $\boldsymbol{E}//\boldsymbol{c}^*(\boldsymbol{k}\perp\boldsymbol{c}^*)$ at the band-edge region and at a constant temperature of 77 K. For both polarizations, $\boldsymbol{E}\perp\boldsymbol{c}^*$ and $\boldsymbol{E}//\boldsymbol{c}^*$, the recorded spectra show two PL bands: (1) a low-intensity band at the low-energy side (2.1–2.3 eV) of the spectra and (2) a high-intensity slightly asymmetric Lorentzian-shaped band at the high-energy side (2.3–2.6 eV). For $\boldsymbol{E}\perp\boldsymbol{c}^*(\boldsymbol{k}//\boldsymbol{c}^*)$ polarization, the low- intensity band was attributed to radiative DAP recombination [1], whereas the recombination mechanism of the high-intensity emission observed at 2.52 eV (denoted as the *H* band in early studies [2, 3] was attributed to excitonic recombination. To the best of our knowledge, there are no reports exist on the PL spectrum of layered $TlInS_2$ compounds for $\boldsymbol{E}//\boldsymbol{c}^*(\boldsymbol{k}\perp\boldsymbol{c}^*)$ polarization. It is important to note that in this polarization, the PL band was centered at an energy (2.49 eV) lower than that of the reported *H* band (2.54 eV [2] and 2.52 eV [3]). For $\boldsymbol{E}\perp\boldsymbol{c}^*(\boldsymbol{k}//\boldsymbol{c}^*)$ polarization, we particularly concentrated on the high-energy side of the PL spectrum (2.3–2.6 eV).

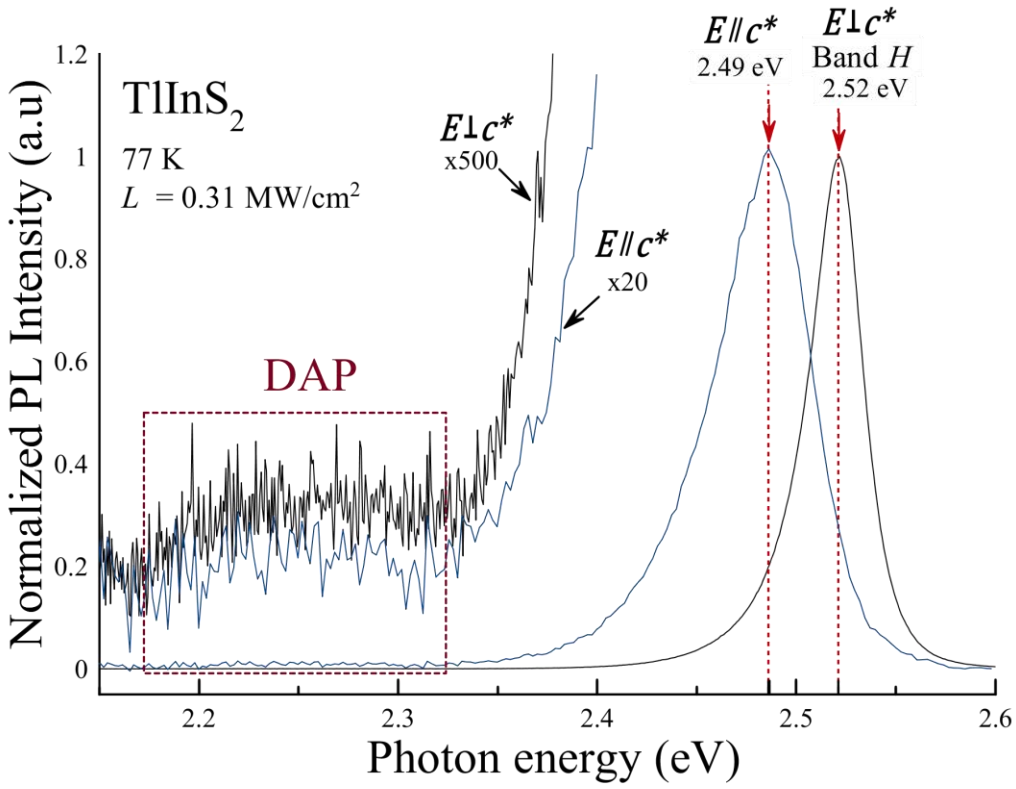

Figure 4.1 PL spectra of $TlInS_2$ for $\boldsymbol{E}\perp\boldsymbol{c}^*(\boldsymbol{k}//\boldsymbol{c}^*)$ and $\boldsymbol{E}//\boldsymbol{c}^*$ $(\boldsymbol{k}\perp\boldsymbol{c}^*)$ polarizations at 77 K and excitation density $L = 0.31$ MW/cm^2.

4.2.1 Excitation dependence of PL spectra

Figure 4.2 shows the excitation density (L) dependence of the PL spectra of $TlInS_2$ single crystals in the band-edge region at a constant temperature of 77 K for $\boldsymbol{E}\perp\boldsymbol{c}^*(\boldsymbol{k}//\boldsymbol{c}^*)$ polarization.

In the excitation density range 0.01–0.1 MW/cm^2 the energy position of the PL peak is approximately 2.52 ± 0.9 meV, which corresponds to the H band observed in previous studies [2, 3]. With increasing L above 0.1 MW/cm^2, the intensity of the PL emission increases rapidly, and the energy position shifts slightly toward the lower-energy side of the spectrum. Since the energy position of the excitonic emission does not depend on L, here, we re-examine the origin of this band H and the energy shift exhibited with increasing L.

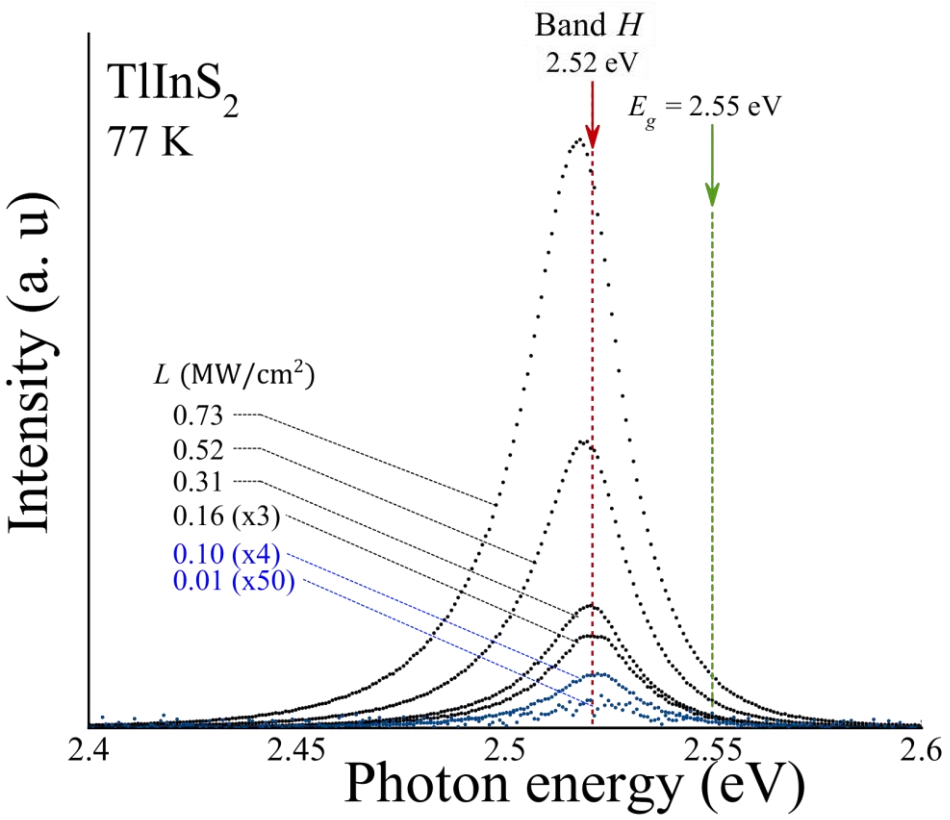

Figure 4.2 Excitation density (L) dependence of PL spectra for $TlInS_2$ crystals at a constant temperature of 77 K for $\boldsymbol{E}\perp\boldsymbol{c}^*(\boldsymbol{k}//\boldsymbol{c}^*)$ polarization.

First, we must verify that the present experiment was performed at low excitation density, for which no screening of the the excitonic interaction occurs and the system does not become metallic. Exciton wave function overlap occurs when the exciton-exciton distance is equal to the exciton diameter; then, the exciton lose their identity as individual quasiparticles and a new collective phase is formed which is known as the electron-hole plasma (EHP). The exciton density at which this occurs is called the Mott density (N_{Mott}) and is given approximately derived from

$$N_{Mott} \cong \frac{1}{a_B^3} \qquad (4.1)$$

where a_B is the Bohr radius of FEs [4]. In the case of $TlInS_2$ crystals, N_{Mott} was calculated to be ~1.76×10^{20} cm^{-3} using a_B ~ 1.79 nm [5].

On the other hand, the concentration level of the created FE N_{FE} (cm^{-3}) [6] is provided by

$$N_{EF} \cong \frac{L}{h\upsilon}\alpha\tau \qquad (4.2)$$

where L (W/cm^2) is the excitation density, $h\upsilon$ (eV) is the excitation energy, α (cm^{-1}) is the absorption coefficient at the excitation energy, and τ (s) is the exciton life time. Considering a maximum density of $L \approx 0.73$ MW/cm^2, $h\upsilon = 3.3$ eV (for a 400 nm laser beam), $\alpha \approx 1.3$ cm^{-1} (at 3.3 eV, 77 K [7]), and $\tau \approx 1$ ns (at 77 K [8]), N_{FE} was estimated to be ~1.79×10^{19} cm^{-3}. Since the obtained values (summarized in Table 4.1) show that N_{Mott} was at least one order of magnitude larger than N_{FE}, the energy shift observed in the PL spectra (Figure 4.2) for L above 0.1 MW/cm^2 was not considered to be caused by EHP. Consequently, the observed peak shift may be due to the appearance of other exciton or excitonic complexes (i.e.s biexcitons) at energies below that of band *H*. Therefore, the PL spectra were analyzed using deconvolution method to obtain the relationship between the excitation power density (L) and the PL emission intensity (I) [9, 10]. In the analysis, we deconvoluted the contours of the obtained PL spectra with a Lorentzian function (peak) using the least-squares approach. The Lorentzian functions and their parameters are shown in Figure 4.3.

Table 4.1 : Estimated values for Mott density and resulting FE density at the highest power density used for exciting $TlInS_2$ in our work ($L \approx 0.73$ MW/cm^2).

N_{Mott} (cm^{-3})	1.76×10^{20}
N_{FE} (cm^{-3})	1.79×10^{19}

First, because the PL corresponded to band *H* (at 2.52 eV) in the excitation density from 0.01 to 0.1 MW/cm^2, the PL spectra in this excitation range were deconvoluted (resolved) using one Lorentzian peak with X = 2.52 eV, as shown in Figure 4.4. Then, the PL spectra were resolved into one, two, and three Lorentzian peaks in the excitation density from 0.16 to 0.73 MW/cm^2, as shown in the Figures 4.5a, 4.5b, and 4.5c, respectively, where one of the peaks correspond to band *H*. The insets show the obtained X values for each excitation density. In addition, numerical values of

the residual sum of squares (RSS) and the coefficient of determination (R^2) extracted from the output file are included in the figures. Here, the best fit was considered as that having the smallest RSS or, equivalently, the largest R^2.

As expected, better results were obtained when the entire PL spectrum was resolved into two and three peaks than when using only one peak. In addition, the inset of Figure 4.5a shows that the peak position (X_H) shift to the low-energy side with increasing L does not correspond to excitonic PL. Therefore, we discarded this result. To obtain de results shown in Figure 4.5b, in the deconvolution analysis, we assumed that these two peaks had fixed position energies: band H at 2.52 eV and band M in the range between 10 and 20 meV, below 2.52 eV. Then, taken into account the obtained RSS and R^2 values of each fit as well as the results of the temperature dependence of the PL spectra that are related to the binding energy (which is explained in section 4.2.2) we determined that the best fit was obtained for peaks spaced at 13.5 meV.

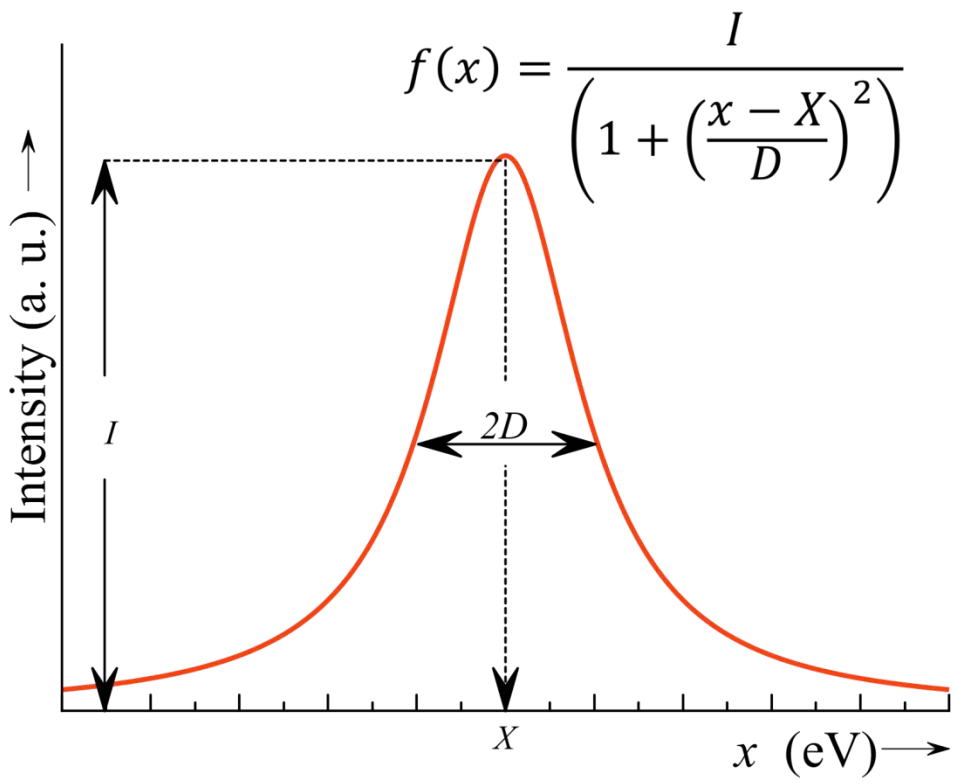

Figure 4.3 The Lorentzian function. Here, I is the maximum intensity, X is the energy position at the maximum intensity, and D is the half width at half maximum (HWHM) i.e., at $I/2$.

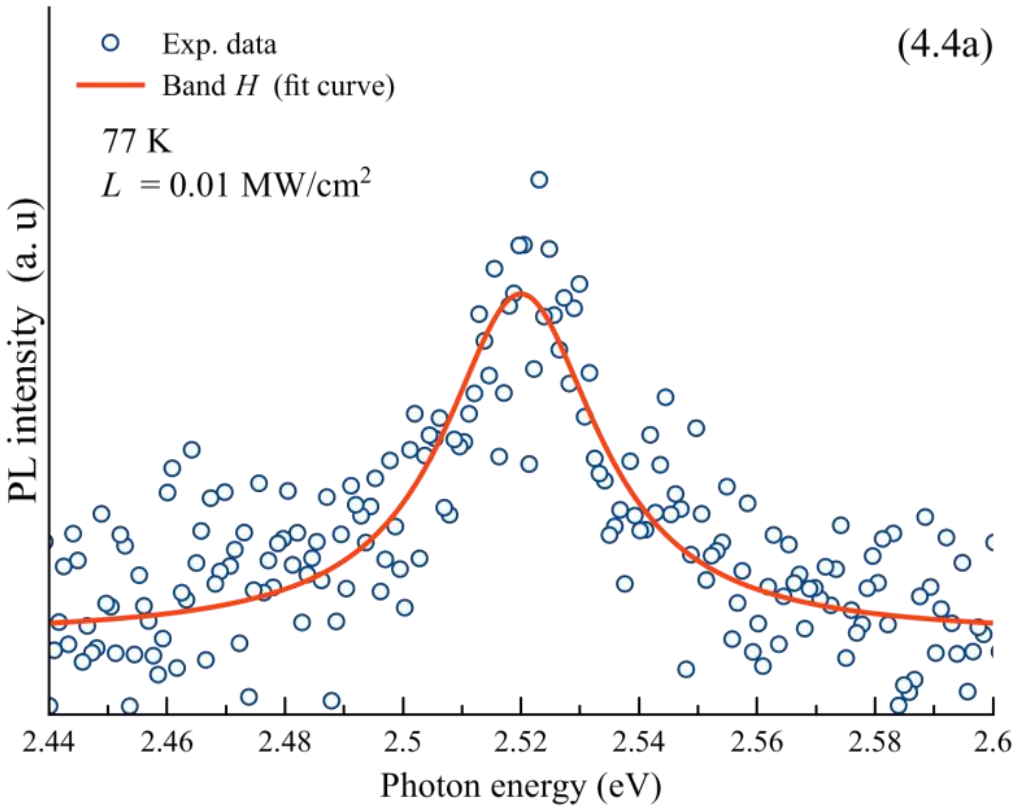
Exp. data
Band H (fit curve)
77 K
L = 0.01 MW/cm2
(4.4a)
PL intensity (a. u)
2.44
2.46
2.48
2.5
2.52
2.54
2.56
2.58
2.6
Photon energy (eV)

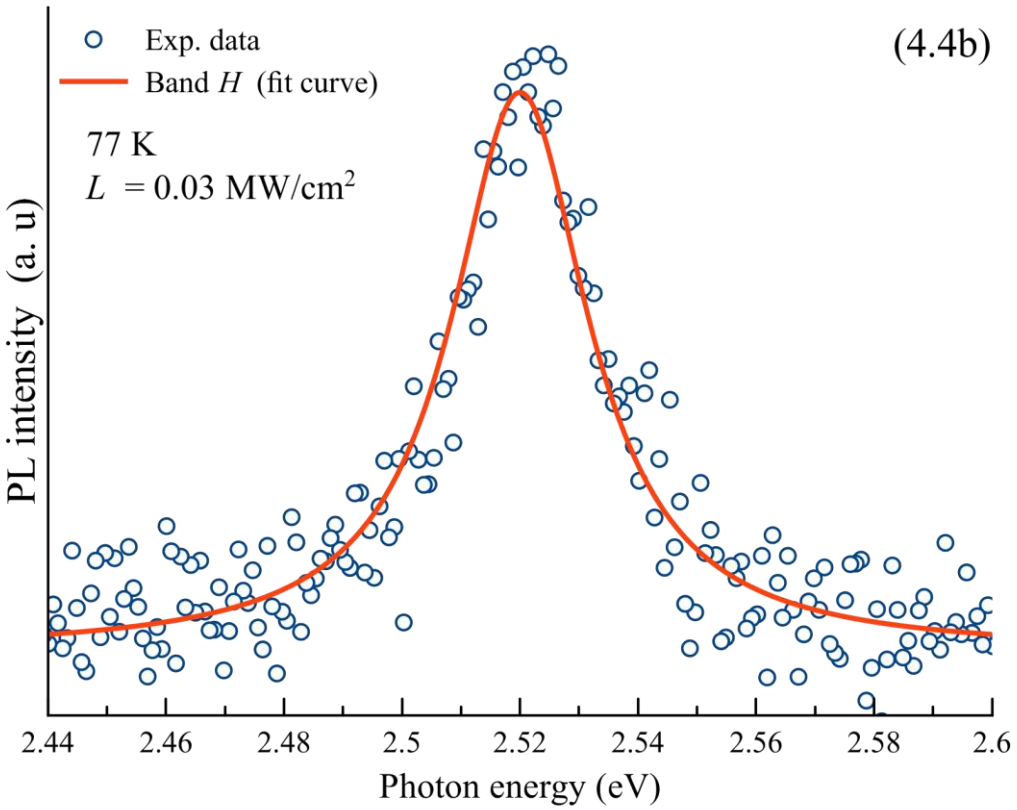
Exp. data
Band H (fit curve)
77 K
L = 0.03 MW/cm2
(4.4b)
PL intensity (a. u)
2.44
2.46
2.48
2.5
2.52
2.54
2.56
2.58
2.6
Photon energy (eV)

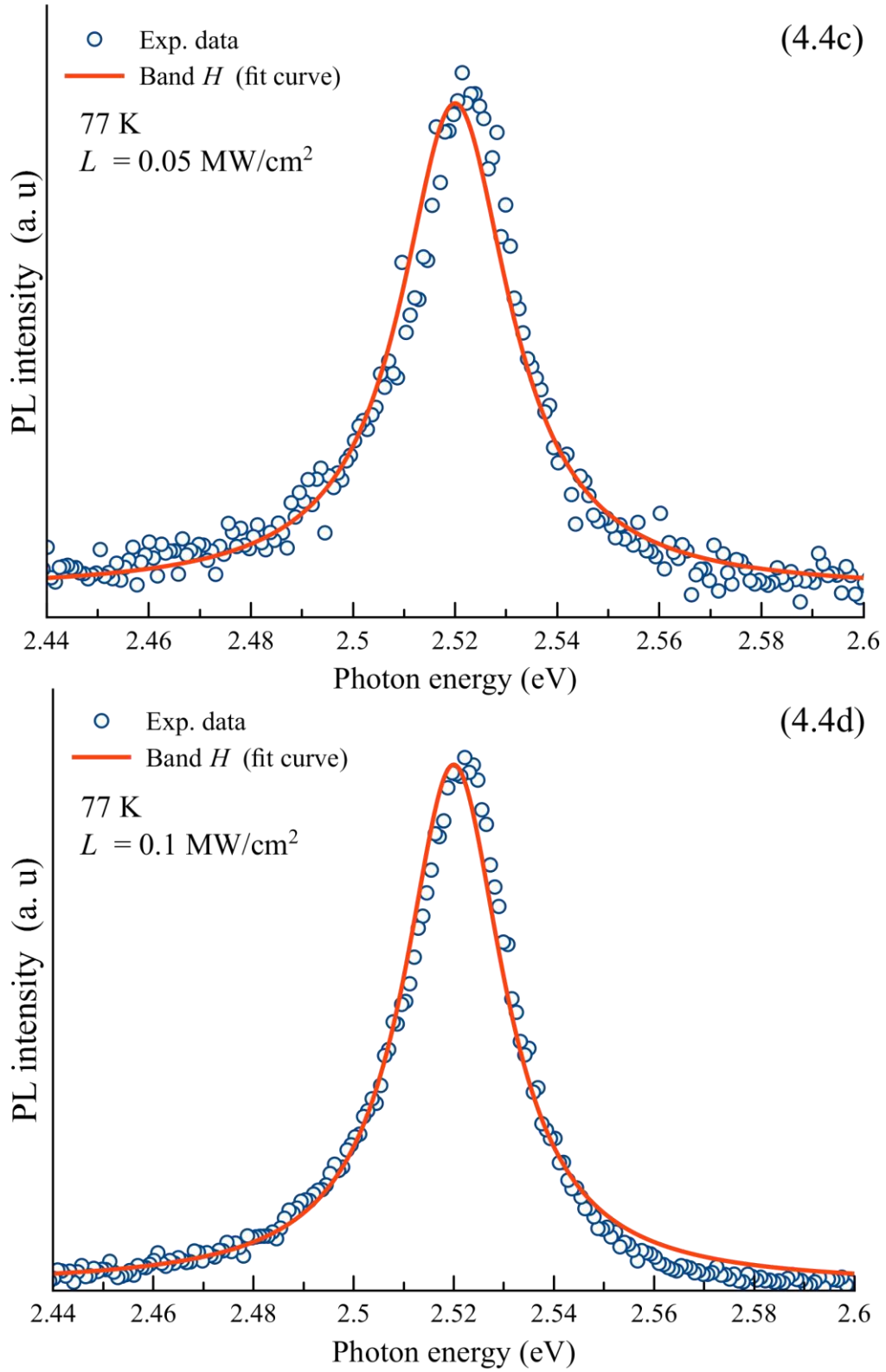

Figure 4.4 Deconvolution of the PL spectra in the excitation density range from 0.01 to 0.1 MW/cm^2. The PL spectra were resolved into one Lorentzian peak with X = 2.52 eV for L = 0.01, 0.03, 0.05, and 0.1 MW/cm^2, which correspond to the excitonic band H.

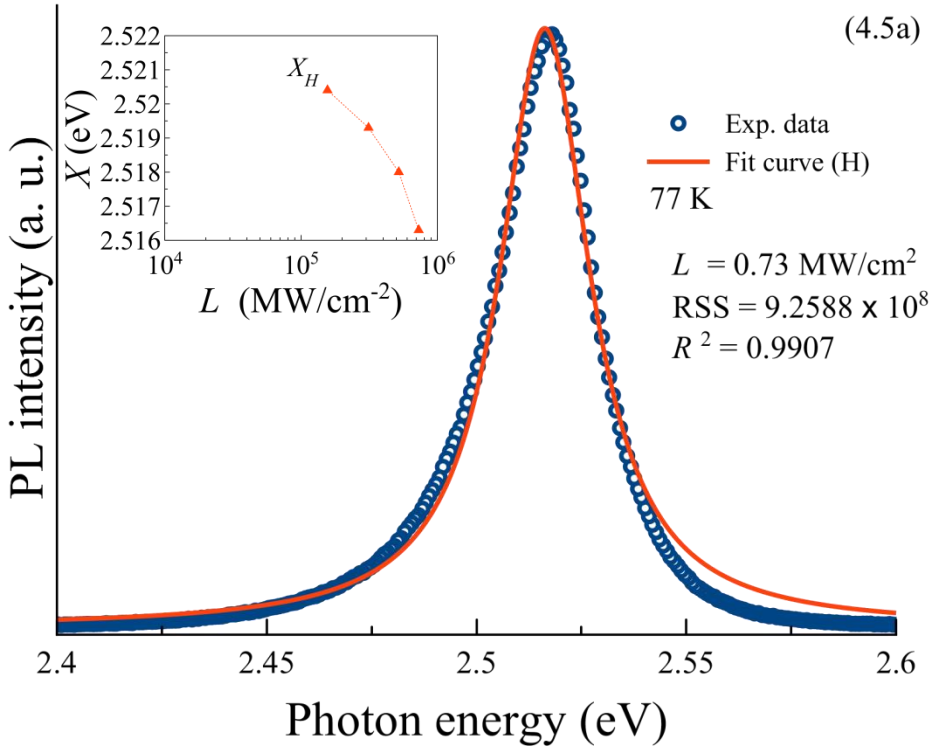
(4.5a)
PL intensity (a. u.)
Photon energy (eV)
2.4
2.45
2.5
2.55
2.6
X (eV)
2.522
2.521
2.52
2.519
2.518
2.517
2.516
X_H
10^4
10^5
10^6
L (MW/cm^{-2})
Exp. data
Fit curve (H)
77 K
L = 0.73 MW/cm^2
RSS = 9.2588 x 10^8
R^2 = 0.9907

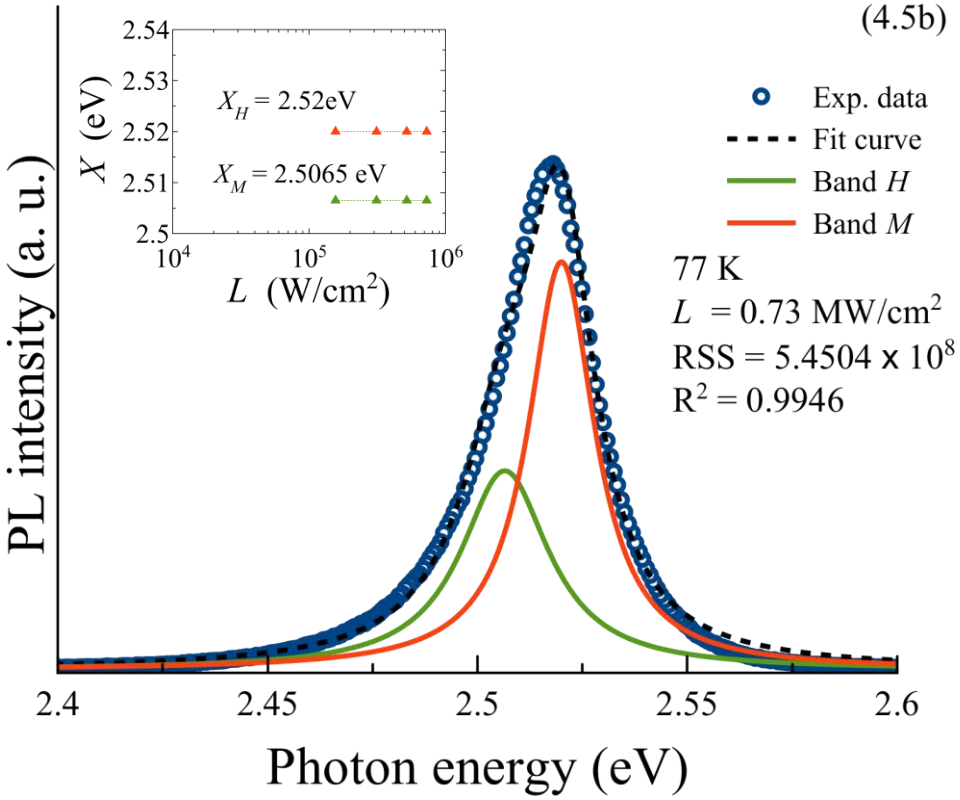
(4.5b)
PL intensity (a. u.)
Photon energy (eV)
2.4
2.45
2.5
2.55
2.6
X (eV)
2.54
2.53
2.52
2.51
2.5
X_H = 2.52eV
X_M = 2.5065 eV
10^4
10^5
10^6
L (W/cm^2)
Exp. data
Fit curve
Band H
Band M
77 K
L = 0.73 MW/cm^2
RSS = 5.4504 x 10^8
R^2 = 0.9946

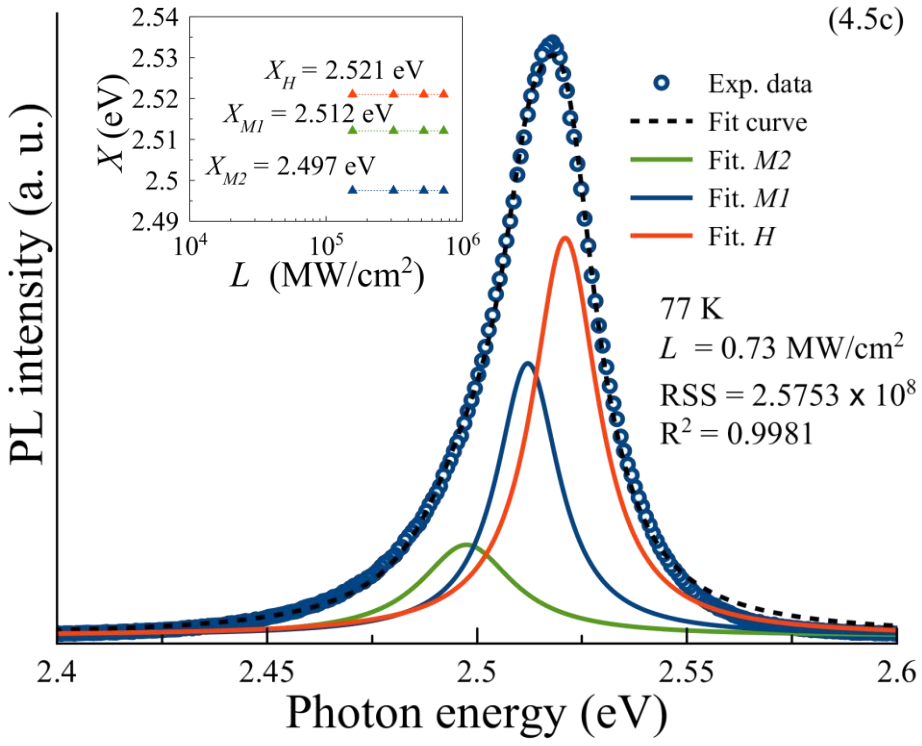

Figure 4.5 Deconvolution of the PL spectra in the excitation density range from 0.16 to 0.73 MW/cm^2. The PL spectra were resolved into one, two and three Lorentzian peaks.

Moreover, the PL spectra could be resolved into three peaks, as shown in the Figure 5.5c. Again, we assumed one peak at 2.52 eV (band *H*) and the other two peaks (M_1 and M_2) at fixed position energies below 2.52 eV. However, the PL spectra deconvolution into three Lorentzian peaks was inappropriate, considering the binding energy of the resulting band M_2, as explained in section 4.2.2.

Subsequently, we focused on the two peaks deconvolution shown in Figure 4.5b. The relationship between L and the intensities of the H and M bands, I_H and I_M, respectively, is shown in Figure 4.6. The calculated I_H and I_M values can be fitted by a simple power form as follows:

$$I \propto L^n \qquad (4.3)$$

where n is a dimensionless exponent [9, 10]. When the excitation energy of the laser light exceeds the gap energy, E_g, the coefficient n is generally $1 < n < 2$ for free- and bound-exciton emissions. Additionally, the radiative recombination of molecular excitons (MEs), called biexcitons, is suggested for the I, which increases approximately as the square of the FE intensity ($\frac{n_{ME}}{n_{FE}} \approx 2$). Using equation 4.3, we determined that the I_H and I_M increase superlinearly, i.e., $n_H \approx 1.7$ and $n_M \approx 3.4$, and the ratio $\frac{n_M}{n_H}$ was calculated to be ~ 2. Thus, the obtained results indicated that the emission bands M and H could be attributed to the radiative recombination of MEs and FEs, respectively. From the peak-to-peak energy difference between M and H bands ($\boldsymbol{X_H - X_M}$), the binding energy of this biexciton was estimated to be ~13.5 meV, as shown in the inset of Figure 4.5b.

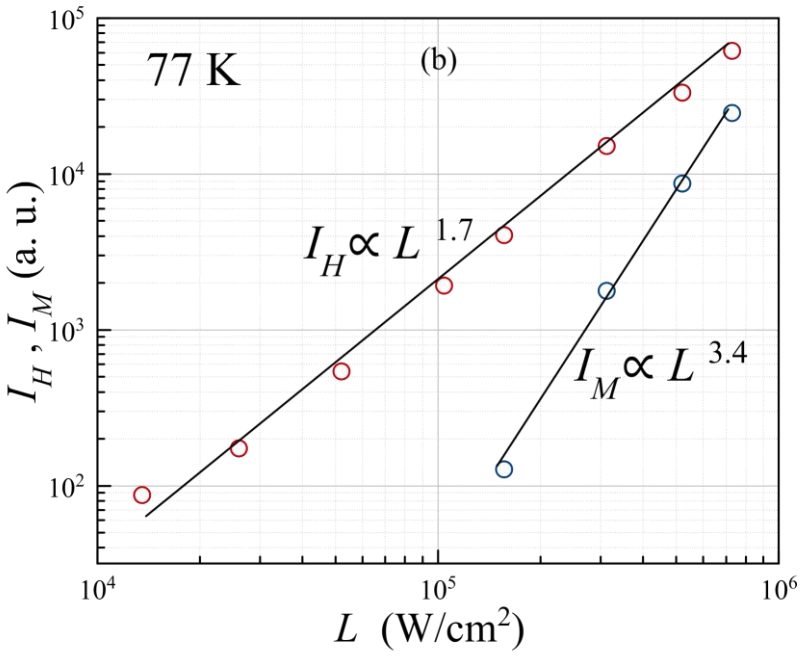

Figure 4.6: The Lorentzian parameters (I) of the deconvoluted H and M bands as a function of excitation density (L).

In most wide-bandgap semiconductors, such as GaN, ZnS, ZnSe, CdS, and $CuGaS_2$, high-density excitons collide with each other and generate MEs (biexcitons) [11]. However, there have been no reports on biexciton luminescence in $TlMeX_2$ compounds. Here, we report the first observation of biexciton luminescence in $TlInS_2$.

4.2.2 Temperature dependence of PL spectra

Next, we analyzed the behavior of the PL spectra as a function of temperature at a constant excitation power density of 0.3 MW/cm^2 in the region 2.2–2.6 eV. The PL spectra of $TlInS_2$ obtained in the temperature range from 77 to 300 K, in which phase transitions (N-I-C) are believed to exist, are shown in Figure 4.7. No appreciable effect of successive thermocycling was observed between the commensurate and normal phases; hence, the results are provided without details regarding their acquisition (i.e., on cooling or heating). The important features of these results are summarized below:

- In the paraelectric phase, a weak, broad, and slightly asymmetric Lorentzia-shaped band appeared at approximately 2.39 eV at 300 K. At lower temperatures, the energy positions of the PL peaks shifted slightly to higher energies (i.e., 2.43 eV at 220 K) and the band intensity increased slowly. The same behavior was observed between 216 and 200 K (I phase).

- At temperatures below ~200 K (ferroelectric-C phase) and down to ~77 K, the energy position of the PL band rapidly shifted to the higher-energy side, and the peak intensity exhibited a strong increase with decreasing temperature.

As in the case of the excitation density dependence, a deconvolution procedure was applied to analyze the behavior of the PL spectra as a function of temperature, and we extracted the X_H and X_M values of the *H* and *M* bands, respectively. In the ferroelectric phase above 77 K, the PL spectra were divided into two Lorentz peaks (*H* and *M* bands) separated by a constant distance of 13.5 meV. We assumed that the binding energy of the FE and ME did not change with temperature. However, at approximately 180 K, the intensity of the biexciton *M* band decreased significantly became and disappeared because the binding energy became comparable with the thermal energy Tk_B, where k_B is Boltzmann's constant (8.617×10^{-5} eV/K) and *T* is the lattice temperature. Therefore, at higher temperatures (I-to-N phase), the PL emission spectrum mainly originates from one band, the excitonic *H* band. The fact that the biexciton emission could be observed up to 160 K (Tk_B = 13.7 meV) supports the hypothesis that the binding energy of this structure is approximately 13.5 meV. In addition, it could explain why the intensity of the entire PL spectra increased rapidly for

temperatures below 200 K (C phase). Moreover, the PL spectra deconvolution in three Lorentzian peaks is inappropriate considering that the binding energy of the resulting band M_2 ($X_H - X_{M2}$ = 24 meV) suggests that this structure should be observed up to 278.5 K; however, was not observed in the temperature dependence of the PL spectra, as shown in Figure 4.7.

The extracted values for the X_H and X_M bands are plotted against the temperature in Figure 4.8. Some differences are observed when we compare our results to those of early studies on the excitonic emission from $TlInS_2$ crystals [2, 3]. As seen in Figure 4.7 for the C phase, the previous studies also reported a rapid energy position shift (labels 1 and 2) and energy values of the *H* band that agree well with those obtained in the present work. However, at high temperatures, the energy values of band *H* (labels 1 and 2) and X_H exhibit strong differences, and there is no longer agreement in the I and N phases. Moreover, the reported anomaly in the temperature range from 195 K to 216 K (I phase), where the energy position of the band *H* is nearly independent of the temperature [3], was not observed in the band *H* energy in this work. We attribute this discrepancy mainly to the difference between the polytypes examined in the early PL studies and those investigated in the present work. Label (3) in figure 4.8, indicates the exciton energy calculated from the deconvoluted imaginary part of the dielectric function obtained by the ellipsometry measurements [12] of $TlInS_2$ in **E**//***c****. Clearly, a rapid energy shift is observed in the C phase with decreasing temperatures; however, the energy values are smaller than those obtained from PL measurements. We attribute these energy differences to the configurations of the experiments (***E***⊥***c**** in this work).

Finally, Label (4) corresponds to the relationship (Equation 1.2) of the bandgap (E_g) and FE (E_{FE}) energies versus the temperature, which was obtained using the Bose-Einstein statistical factor [7]. The exciton energy calculated using Equation 3 and the parameters presented in Table 4.2 shows the best agreement with the experimental data at temperatures below 100 K (C phase), while a significant deviation is observed in the I and N phases. Therefore, this treatment may not be adequate in the extended temperature range of N-I-C phase transitions. For comparison, Table 4.2 also shows the parameters calculated by the least-squares fitting of the experimental energy position of band *H* using Equation 1.2 in the ferroelectric-C phase in the region 77–200 K.

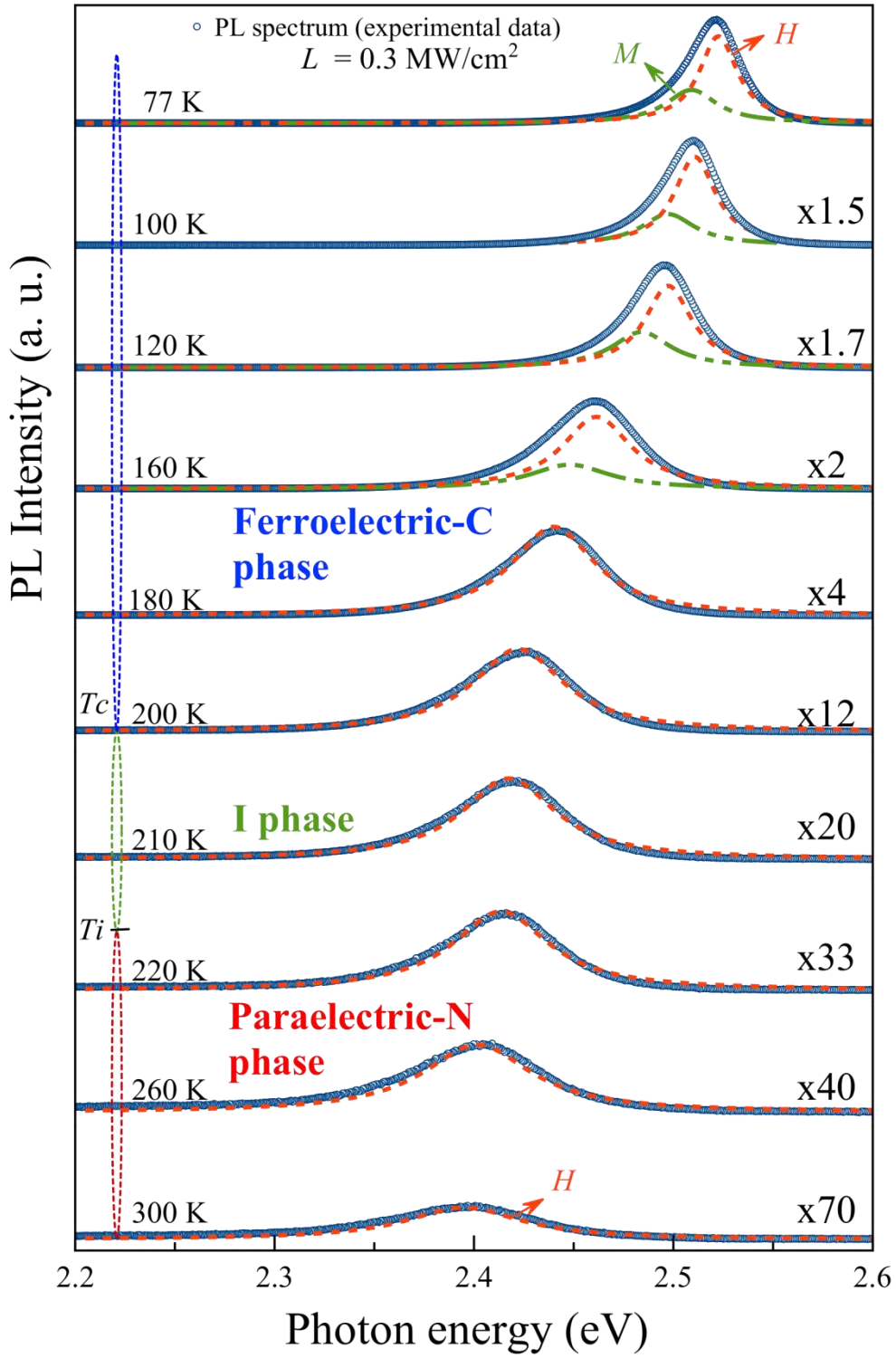

Figure 4.7 PL spectra of $TlInS_2$ crystal at different temperatures in the range 77–300 K under a constant excitation power density of 0.3 MW/cm^2.

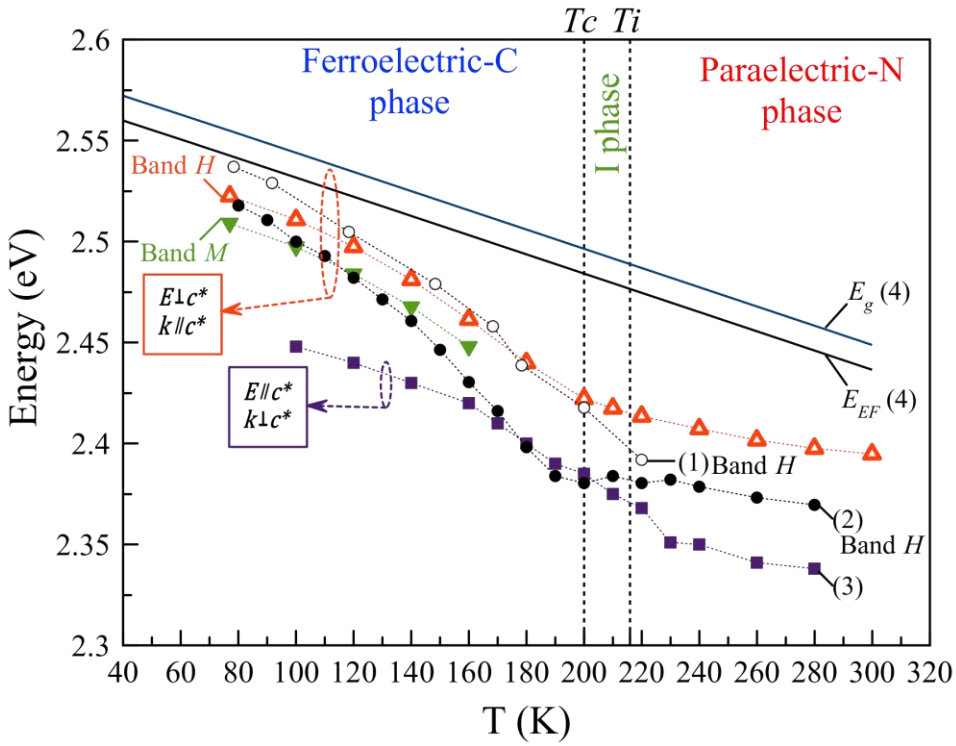

Figure 4.8: Temperature dependence of the energy position of the PL *H* and *M* bands.

Table 4.2: Values of the Bose-Einstein statistical relation parameters.

E_B (eV)	α_B (eV)	Θ_B (K)	E_i (eV)
2.592	0.0062	26	0.0123
$E_B - E_i = 2.71$	0.179	292.9	-

4.3 PL spectra of $TlGaSe_2$

To date, many studies have examined layered $TlGaSe_2$ crystals, which belong to the group of quasi-two-dimensional $TlMeX_2$ compounds. However, besides photoconductivity [73] and optical absorption [74], the excitonic properties of $TlGaSe_2$ are not well understood. The reported photoconductivity and optical absorption data showed that excitons are located at 2.13 eV [73] and 2.12 eV [74], respectively, at low temperatures.

4.3.1 Excitation dependence of PL spectra

Figure 4.9 shows the PL spectra of $TlGaSe_2$ for light polarization $\boldsymbol{E}\perp\boldsymbol{c}^*(\boldsymbol{k}//\boldsymbol{c}^*)$ and $\boldsymbol{E}//\boldsymbol{c}^*(\boldsymbol{k}\perp\boldsymbol{c}^*)$ at the band-edge region and a constant temperature of 77 K. The optical transitions responsible for PL emission near the band edge are obviously polarized for $\boldsymbol{k}\perp\boldsymbol{c}^*$ ($\boldsymbol{E}//\boldsymbol{c}^*$ and $\boldsymbol{E}//\boldsymbol{c}^*$). Because, FEs may responsible for the emission from $TlGaSe_2$ observed at $\boldsymbol{E}//\boldsymbol{c}^*$, we consider the PL spectra in more detail.

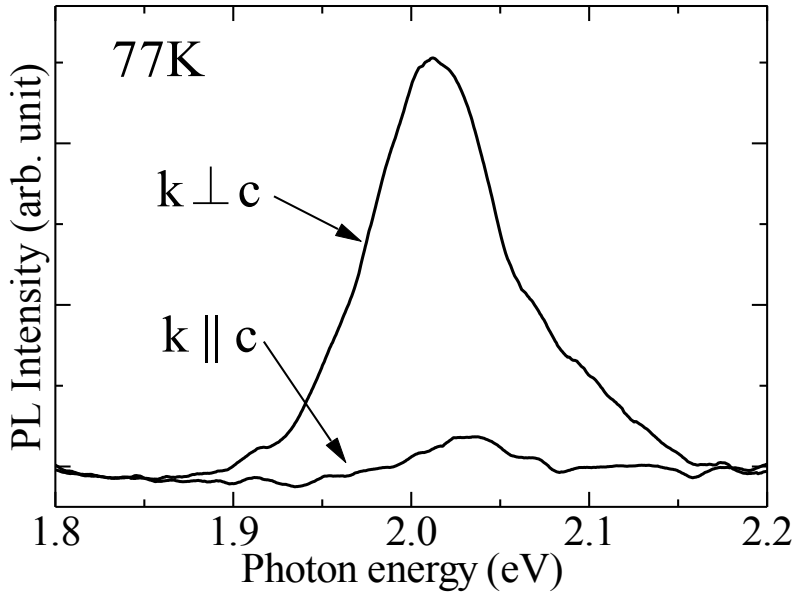

Figure 4.9 PL spectra of $TlGaSe_2$ for $\boldsymbol{k}//\boldsymbol{c}^*$ and $\boldsymbol{k}\perp\boldsymbol{c}^*$ at 77 K.

The PL spectrum for $\boldsymbol{E}//\boldsymbol{c}^*(\boldsymbol{k}\perp\boldsymbol{c}^*)$, shown in Figure 4.9, is slightly asymmetric Gaussian-shaped band and exhibits a tail on the high-energy side, which obviously

means that the spectrum includes more than one peak. Therefore, we deconvoluted the spectrum (Figure 4.10) and then resolved resolved it into two Gaussian peaks, denoted as A and B bands, located at 2.01 and 2.10 eV, respectively. Figure 4.11 shows the excitation intensity dependence of the emission intensities of peaks A and B at 77 K, which is very well described by Equation 4.3. For peaks A and B, $n_A \approx 1.9$ and $n_B \approx 1.8$, respectively. At low excitation density, the emission intensity of the deconvoluted peak B is very low. Therefore, the accuracy of the n_B value for peak B is low. Because the exponent n_B for peak B is quite large ($n_B > 1$), and the peak energy is very close to that of FEs observed via optical absorption [13] and photoconductivity [14] spectra, we assigned peak B to FE emission in the $TlGaSe_2$ crystals. The n_A value for peak A (1.9) is also rather large and nearly equal to that of peak B. This means that peak B has the same recombination mechanism as peak A. Consequently, the recombination mechanism for peak A must also be the irradiative decay of FEs.

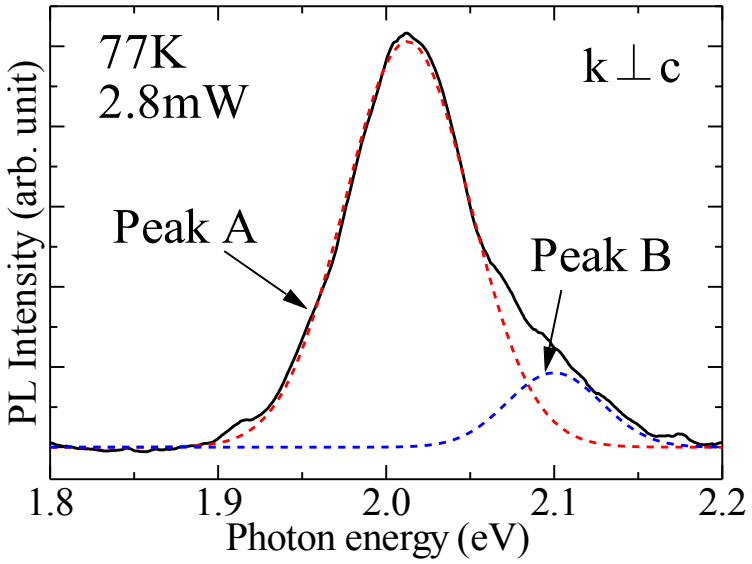

Figure 4.10 PL spectrum of $TlGaSe_2$ measured at 77 K.

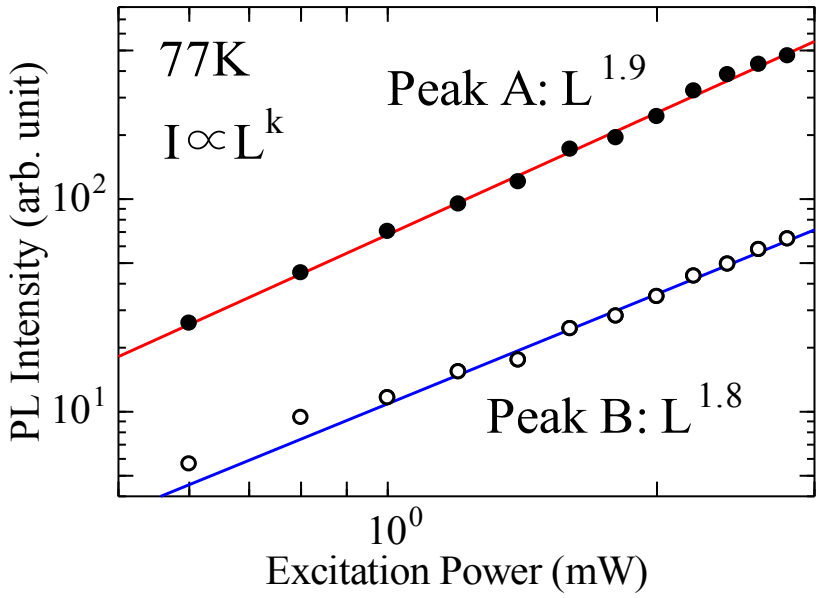

Figure 4.11 Excitation intensity dependence of the emission intensities of peaks A and B in the $TlGaSe_2$ spectrum measured at 77 K.

Because the structure of $TlGaSe_2$ includes defects, the perfect stacking between layers is largely disrupted; thus, the monoclinic ***b*** axis and the ***a*** axis mix and exchange positions [15]. We believe that the A excitons resulted from the defective volume fraction of the studied crystals.

4.3.2 Temperature dependence of PL spectra

Next, we analyzed the behavior of the PL spectra as a function of temperature at a constant excitation power density of 5 mW in the region 2.8–2.2 eV. The PL spectra of $TlGaSe_2$ obtained in the temperature range from 77 to 300 K, in which phase transitions (N-I-C) are believed to exist, are shown in Figure 4.4. As no appreciable effect of successive thermocycling between the commensurate and normal phases was observed, the results are provided without details regarding their acquisition (i.e., cooling or heating).

Figure 4.12 shows the PL spectra at 77, 120, and 160 K. The temperature dependence of the emission energy of peaks A and B at temperatures ranging from 77 to 300 K is shown in Figure 4.10. With increasing temperature, the intensity of peak B

decreases compared to that of peak A, and peak B disappears at temperatures above 160 K. The width of the PL spectra also increases with increasing temperature. The intensity of the deconvoluted peak B is rather low in the high-temperature range. Therefore, peak B may be screened by thermal effects. However, peak A, which is located at 2.01 eV, remains at room temperatures and is observed to change very little with varying temperature. We can estimate the bandgap change of $TlGaSe_2$ as a function of temperature by using peak A instead of the pure FE, peak B. Thus, the bandgap also changes very little with temperature.

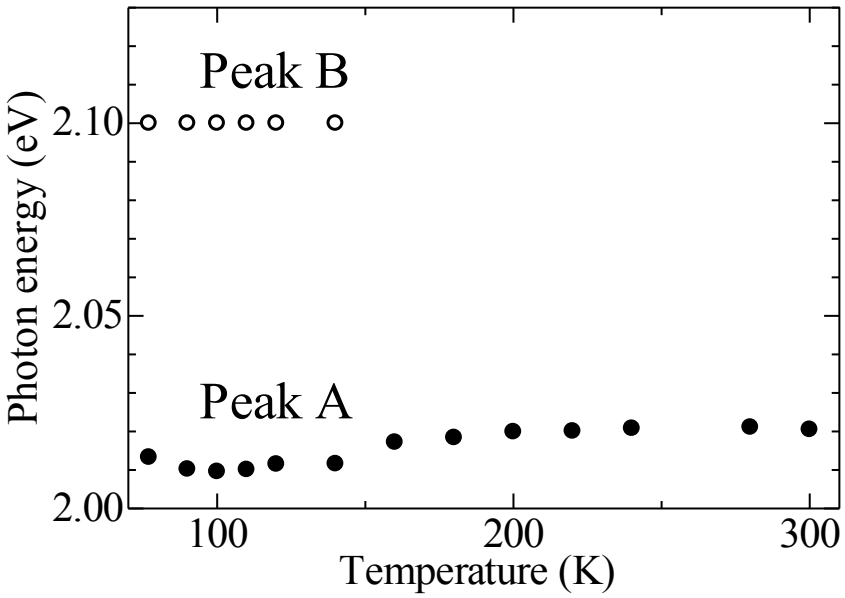

Figure 4.10 Emission energy of peaks A and B in the $TlGaSe_2$ spectrum between 77 and 300 K.

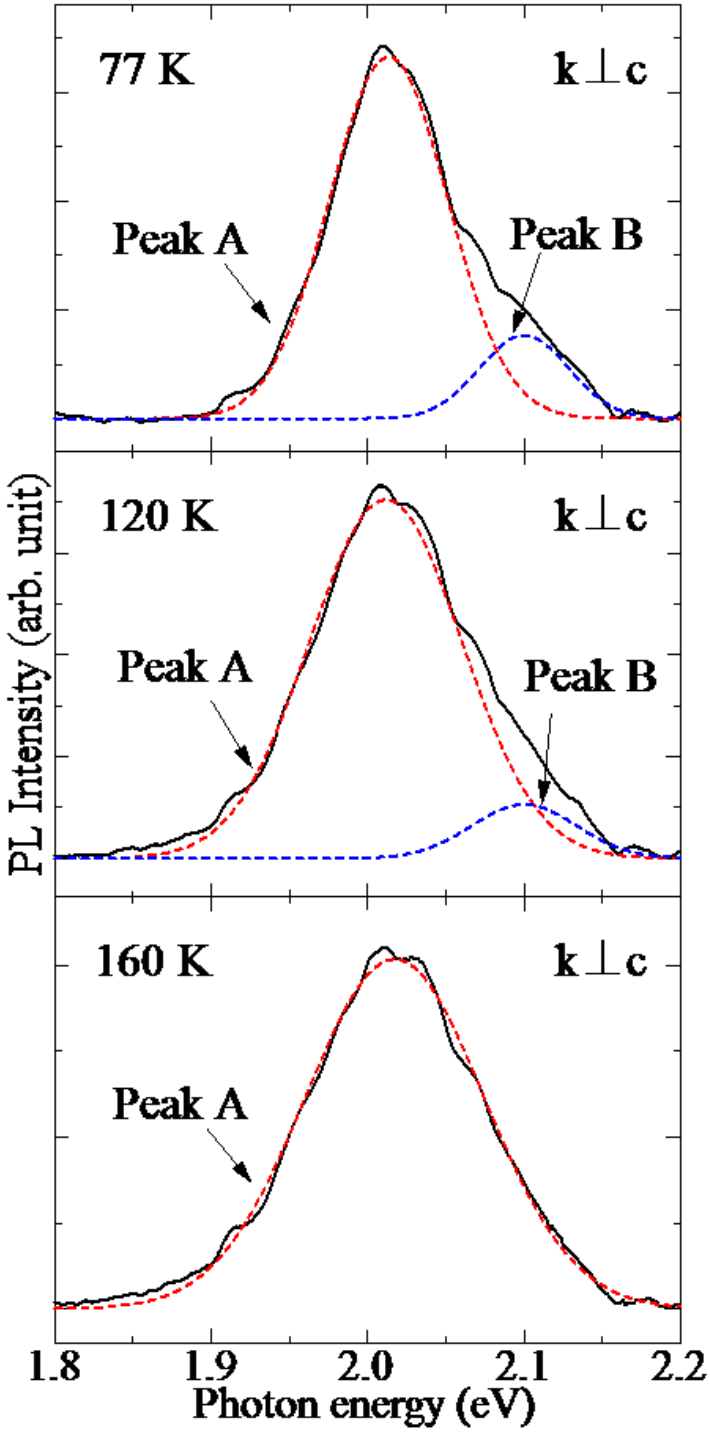

Figure 4.12 at Temperature dependence of PL intensity of the $TlGaSe_2$ for ***E***//***c****(***k***⊥ ***c****) at 77 K.

4.4 Summary

We investigated the PL spectra of $TlInS_2$ crystals using a confocal microscopy system. For $\boldsymbol{E}\perp\boldsymbol{c}^*(\boldsymbol{k}//\boldsymbol{c}^*)$ light polarization, a strong PL band was observed in the entire temperature range from 77 to 300 K, over which a series of phase transitions is believed to occur. At 77 K (ferroelectric-C phase) and under excitation densities above 0.7 MW/cm^2, the PL spectrum consisted of two components: (1) FE luminescence (*H* band) and (2) biexcitons luminescence (*M* band). The binding energy of the biexcitons was estimated to be ~13.5 meV, and the structure dissociated at temperatures between 140 and 160 K. For higher temperatures, up to 300 K, the crystal phase changed to a paraelectric-N phase state through an intermediate I phase, and the PL spectra consisted mainly of FE emission (*H* band). To the best of our knowledge, this is the first observation of biexcitonic emission in the PL spectra of $TlInS_2$ crystals.

Furthermore, we investigated the PL spectra of $TlGaSe_2$ using confocal microscopy. The PL spectra appeared only for the $\boldsymbol{k}\perp\boldsymbol{c}$ configuration. The spectra, which were asymmetric, were separated into two Gaussian peaks, A and B, located at 2.01 and 2.10 eV, respectively. By analyzing the excitation intensity dependence of the PL intensity and previously reported data, we attributed peak B to pure FE emission from the $TlGaSe_2$ crystals. This is the first observation of FEs in $TlGaSe_2$ using PL measurements. Peak A was also assigned to Fes; however, its FE emission could originate from crystals in which mixed and exchanged ***a*** and ***b*** axis, or to layers that were stacked with a shift to the parallel (***ab*** plane).

References

[1] A. Aydinli, N. N. Gasanly, I Yilmaz, and A. Serpenguzel, Semicond. Sci. Technol. 14, pp. 599–603 (1999).

[2] K. R. Allakhverdiev, M. N. Gasanly, and A. Aydinli, Solid State Comm., vol. 94, pp. 777–782 (1995).

[3] T. Arai et al., Ternary and Multinary Compounds in the 21st Century, IPAP Books 1, pp. 24–32 (2001).

[4] C. F. Klingshirn, Semiconductor Optics, Springer-Verlag, Berlin, (1997).

[5] M. Y. Bakirov, N. M. Zeinalov, S. G. Abdullayeva, V. A. Gajiyev, and E. M. Gojayev, Solid State Comm., vol. 44, 2, pp. 205–207 (1982).

[6] I. Pelant and J. Valenta, Luminescence Spectroscopy of Semiconductors, Oxford University Press, (2012).

[7] J. A. Kalomiros and A. Anagnostopoulos, Phys. Rev. B, vol. 50, pp. 7488–7494 (1994).

[8] K. Wakita, K. Nishi, Y. Ohta, and G. Hu, J. Phys. Chem. Solids, vol. 64, pp. 1973–1975 (2003).

[9] J. I. Pankove, Optical Processes in Semiconductor, Prentice-Hall, (1971).

[10] T. Schmidt, K. Lischka, and W. Zulehner, Phys. Rev. B, vol. 45, pp. 8989–8994, (1992).

[11] K. Tanaka, H. Uchiki, S. Iida, T. Terasako, and S. Shirakata, Solid State Comm, vol. 114, 4, pp. 197–201 (1999).

[12] N. Mamedov, Y. Shim, W. Okada, R. Tashiro, and K. Wakita, Phys. Stat. Sol. B, vol. 252, pp. 1248–1253 (2015).

[13] S. G. Abdullayeva, N. T. Mamedov, G. L. Belenky, and M. O. Godzhaev, Phys. Status Solidi B, vol. 103, p. k61 (1981).

[14] O. Z. Alekperov, J. Phys., vol. 64, p. 1707 (2003).

[15] V. Grivickas et al., Phys. Status Solidi B, vol. 244, 4624–4628 (2007).

CHAPTER 5

Raman spectroscopy of $TlInS_2$ single crystal

5.1 Introduction

This chapter describes the Raman scattering spectra of quasy-two-dimensional ternary thallium dichalcogenide $TlInS_2$ and $TlGaSe_2$ usign a confocal microscope system in the temperature range from 77 to 320 K, in which a series of phase transitions is believed to occur.

5.2 Unpolarized Raman scattering spectra

5.2.1 Unpolarized Raman scattering spectra of $TlInS_2$

Figure 5.1 displays, the Raman spectra of $TlInS_2$ at 300 and 77 K in the frequency region of 120–400 cm^{-1}. Each mode in the measured Raman spectra was deconvoluted into Lorentzian peaks (Figure 4.3), using a least squares procedure. The spectra at 300 K exhibit seven Raman peaks, whereas the number of peaks increases to ten at 77 K. Thus, a decrease of the temperature to 77 K generates a variation in the spectra, with an increase of the number brings about a variation in the spectra, such that there is an increase of the number of Raman lines and more distinct separation of closely spaced lines. Furthermore, shifting and broadening of the Raman-active modes are observed with increasing temperature. The frequencies of the observed Raman-active modes are listed in Table 5.1. The frequencies of the modes at 77 and 300 K agree well with those reported previously [1–3]. The table also includes a comparison between the frequencies of the modes observed in the 300 K spectra and those obtained in earlier work [2].

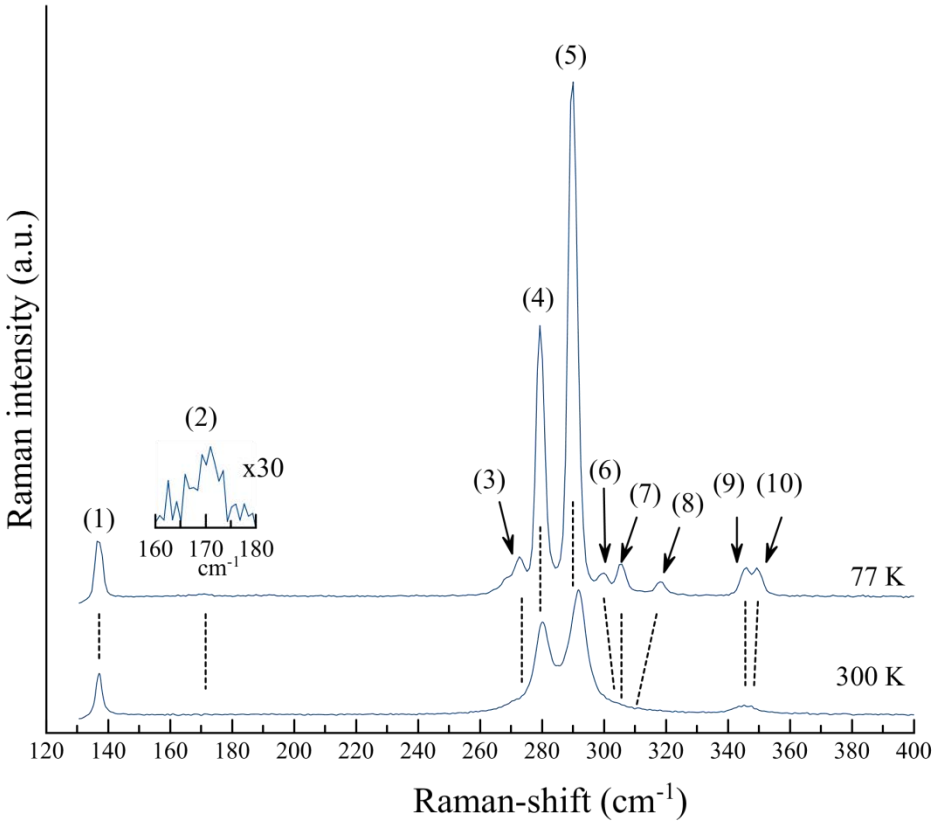

Figure 5.1 Unpolarized Raman spectra of $TlInS_2$ at 300 and 77 K. The numbers correspond to those listed in Table 5.1.

Table 5.1 Raman frequencies (ν_i) in the range 130–400 cm^{-1}.

	This work ν_i (cm^{-1})		**Ref. [2] ν_i (cm^{-1})**
Raman line	**77 K**	**300 K**	**300 K**
(1)	137.7	137.2	138.1
(2)	172.6	175.1	-
(3)	271.9	270.6	272.0
(4)	279.7	280.5	283.2
(5)	290.1	292	294.3
(6)	300.4	-	-
(7)	305.8	309.1	304.5
(8)	318.4	-	-
(9)	345.8	345.5	345.8
(10)	349.9	-	-

5.2.1 Temperature dependence of wavenumber and linewidth

Figure 5.2 presents, the temperature dependence of the peak position (x_0). With decreasing temperature, the Raman peaks with frequencies between 300 and 350 cm^{-1} begin to split. The mode at 300 cm^{-1} is divided into three modes (6, 7, and 8), whereas that at 350 cm^{-1} has two modes (9 and 10) at approximately 225 K and 260 K, respectively. A similar behavior of high-frequency lattice modes was also observed in $TlGaS_2$ [4]. More details on the temperature dependence of the x_0 and γ of the Raman lines are provided in Figure 5.3.

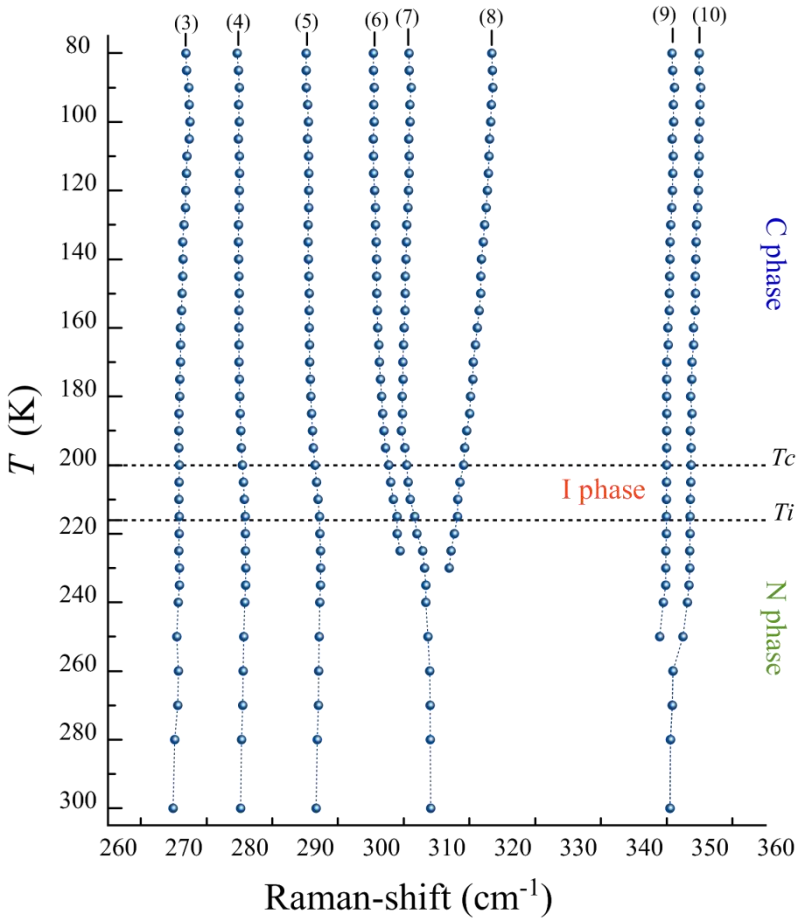

Figure 5.2 Temperature dependence of the mode frequencies of the Raman spectra of $TlInS_2$. The dashed lines represent guides for the eyes. The numbers correspond to those listed in Table 5.1.

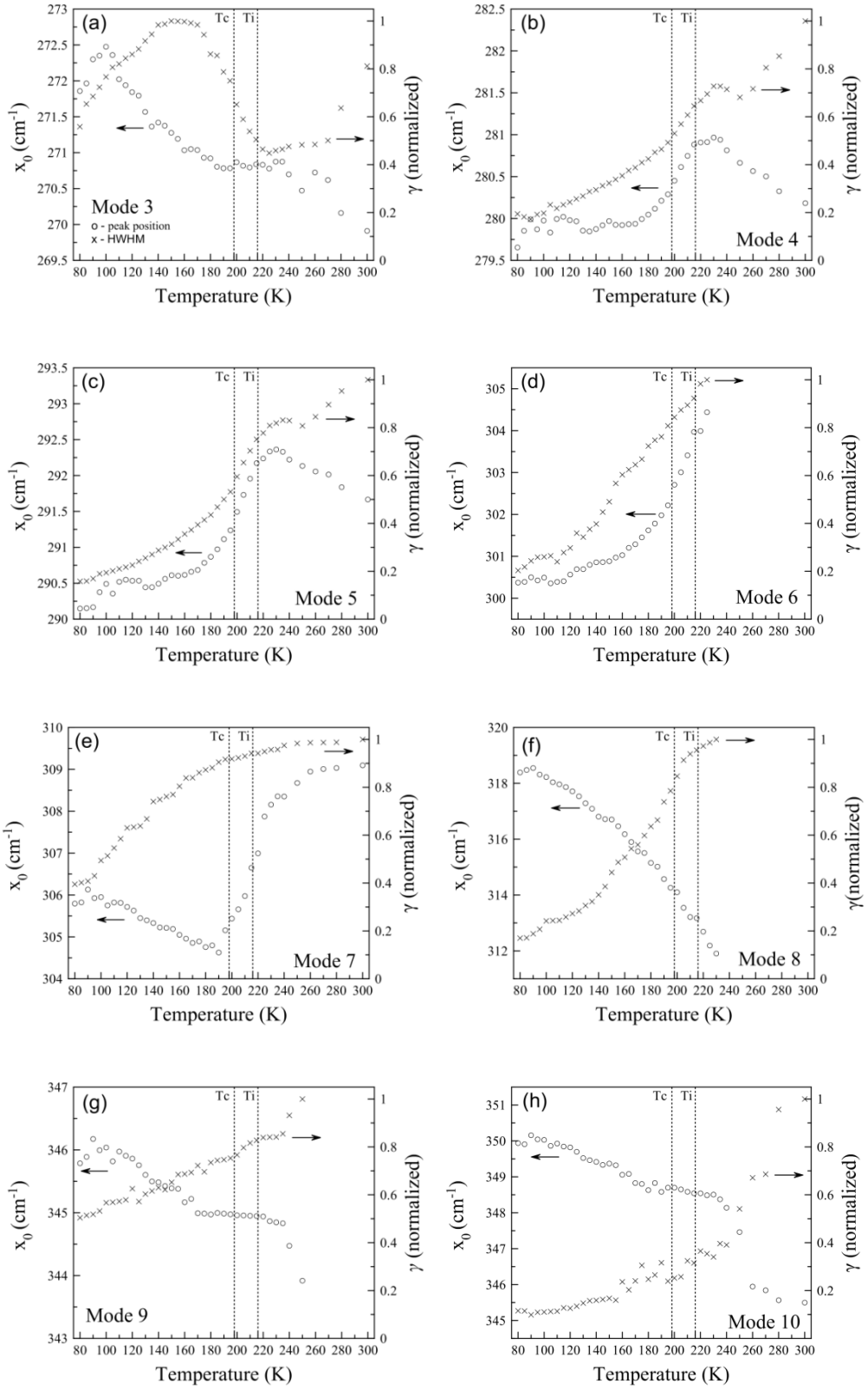

Figure 5.3 Temperature dependence of the x_0 and γ values of the Raman lines.

A distinct feature of the plots of Figure 5.3 is the irregular dependence of x_0 and γ on temperature. This dependence lies beyond the Bose–Einstein distribution for phonons; therefore, it is bound to phase transitions. For example, the x_0 value of mode 3 (Figure 5.3a) initially increases, then suddenly decreases, and finally increases again with increasing temperature. For this mode, x_0 reaches a maximum at 90 K and a bend between 200 and 260 K.

The behavior of mode 5, shown in Figure 5.3c, also exhibits and irregular dependence of x_0 on the temperature. A clear maximum is observed at approximately 225 K. This behavior does not coincide with that reported in [25], where x_0 exhibits changes at high frequencies as the temperature increases from 77 to 300K. A similar behavior of γ and x_0 is observed in the other modes shown in Figure 5.3.

The appearance and disappearance of Raman modes and the irregular behavior of the temperature dependence of the Lorentzian parameters may be due to a structural phase transition. This is because such transition can cause the unit cell to quadruple in the direction of the ***c*** axis in the ferroelectric-C phase. This phenomenon is known as superlattice formation.

5.2.2 Unpolarized Raman scattering spectra of $TlGaSe_2$

The Raman spectra of a $TlGaSe_2$ crystal at 78 and 300 K are shown in Figure 5.4. In the frequency region 50–300 cm^{-1}, the spectra exhibit at least 12 Raman modes at 300 K and this number increases to 17 at 80 K. Table 5.2 summarizes the numerical values of the mode frequencies shown in Figure 5.4 and includes Raman peaks reported by other researches [1, 5] in the frequency range of 50–300 cm^{-1}. Each mode in the measured Raman spectra was deconvoluted into Lorentzian peaks (Figure 4.3), using a least squares procedure. The temperature dependence of the modes is shown in Figure 5.5. As the temperature decreases, additional Raman lines suddenly appear at frequencies of approximately 56, 82, 199, and 237 cm^{-1}, which is an indication of a structural phase transition at low temperatures [1, 4]. More details on the temperature dependence of the frequency and width (FWHM) of the lines are provided in Figure 5.6. We can clearly observe that in the temperature interval between Tc = 107 K and Ti = 120 K, where the phase transition occurs, the temperature dependence of the phonon frequency and the width of the peak show discontinuities for the highest intensity Raman modes (1, 9, 11, and 17).

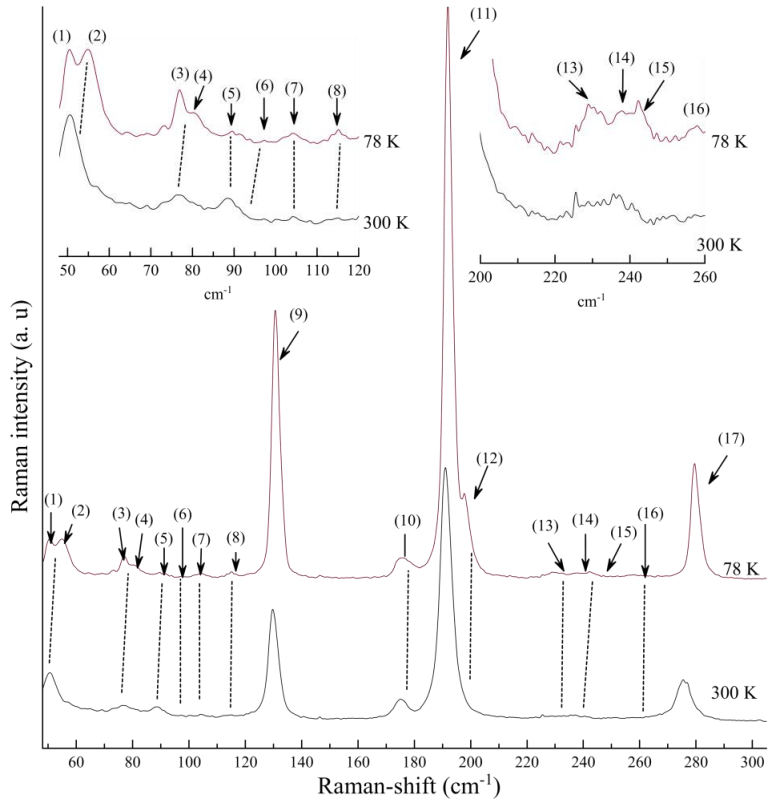

Figure 5.4 Raman spectra of $TlGaSe_2$ at 78 and 300 K. The numbers correspond to those listed in Table 5.2.

These results partly agree with those reported previously [6], where pressure the dependence of phonon frequencies in $TlGaSe_2$ also showed discontinuities for modes 1, 11 and 17. Furthermore, in Figure 5.6 we can also observe that the mode width (FWHM) exhibits broadening with increasing temperature. This explains why Raman modes are clearly resolved at low temperatures, while some closely spaced modes are not resolved at high temperatures

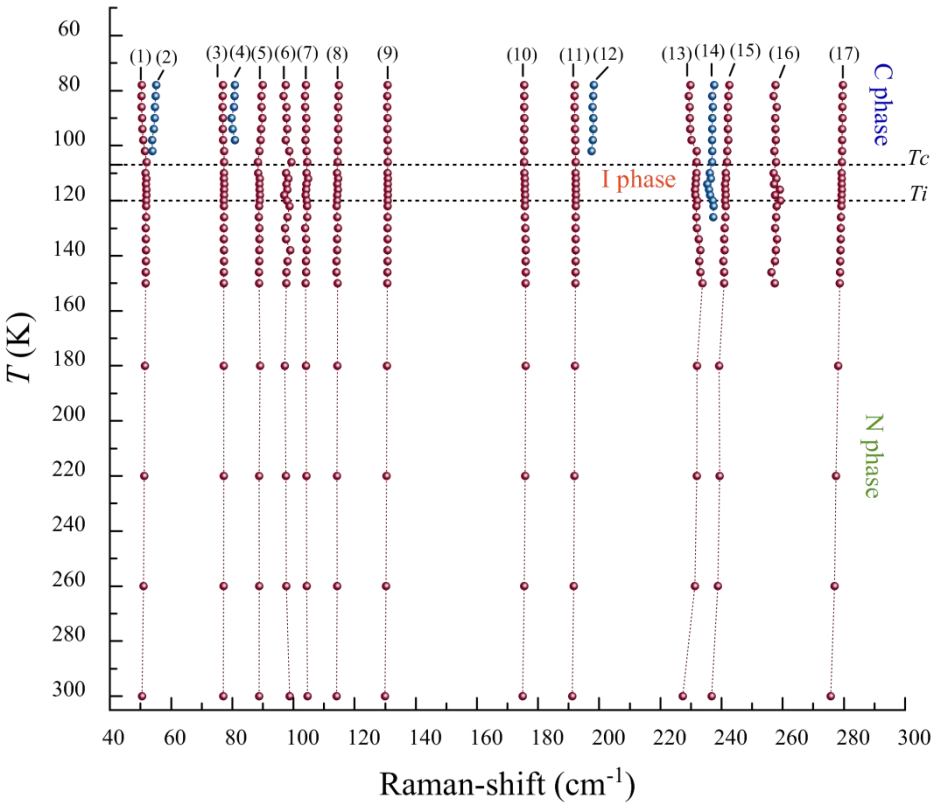

Figure 5.5 Temperature dependence of the mode frequencies of the Raman spectra of $TlGaSe_2$. The dashed lines are guides for the eyes. The numbers correspond to those listed in Table 5.2.

Table 5.2 Raman mode frequencies (v_i) in $TlGaSe_2$ at low and room temperature.

Raman line	Ref. [1] v_i (cm^{-1}) 85 K	Ref. [1] v_i (cm^{-1}) 300 K	Ref. [2] v_i (cm^{-1}) 300 K	Ref. [5] v_i (cm^{-1}) 300 K	This work v_i (cm^{-1}) 80 K	This work v_i (cm^{-1}) 300 K
(1)	53	54	54	53	50.4	50.5
(2)	56	-	-	-	55.1	-
-	74	-	-	-	-	-
(3)	79	-	-	-	78.9	77.1
(4)	83	82	82	80	80.8	-
(5)	87	88	88	-	89.9	88.8
-	92	-	-	91	-	-
(6)	-	-	-	-	97.4	98.8
(7)	106	105	105	105	104.1	104.6
(8)	118	-	-	-	114.9	114.1
(9)	133	133	133	132	130.8	129.9
-	-	-	163	-	-	-
(10)	-	-	-	177	175.5	174.9
(11)	194	194	194	193	192.0	191.2
(12)	199	198	198	-	198.2	-
-	204	-	-	-	-	-
(13)	231	230	230	229	229.8	227.2
(14)	240	240	240	-	237.6	-
(15)	244	-	-	-	242.5	236.8
-	250	250	250	249	-	-
(16)	260	-	-	-	257.6	-
-	-	268	268	-	-	-
(17)	280	278	278	278	279.7	275.7
-	285	-	-	-	-	-

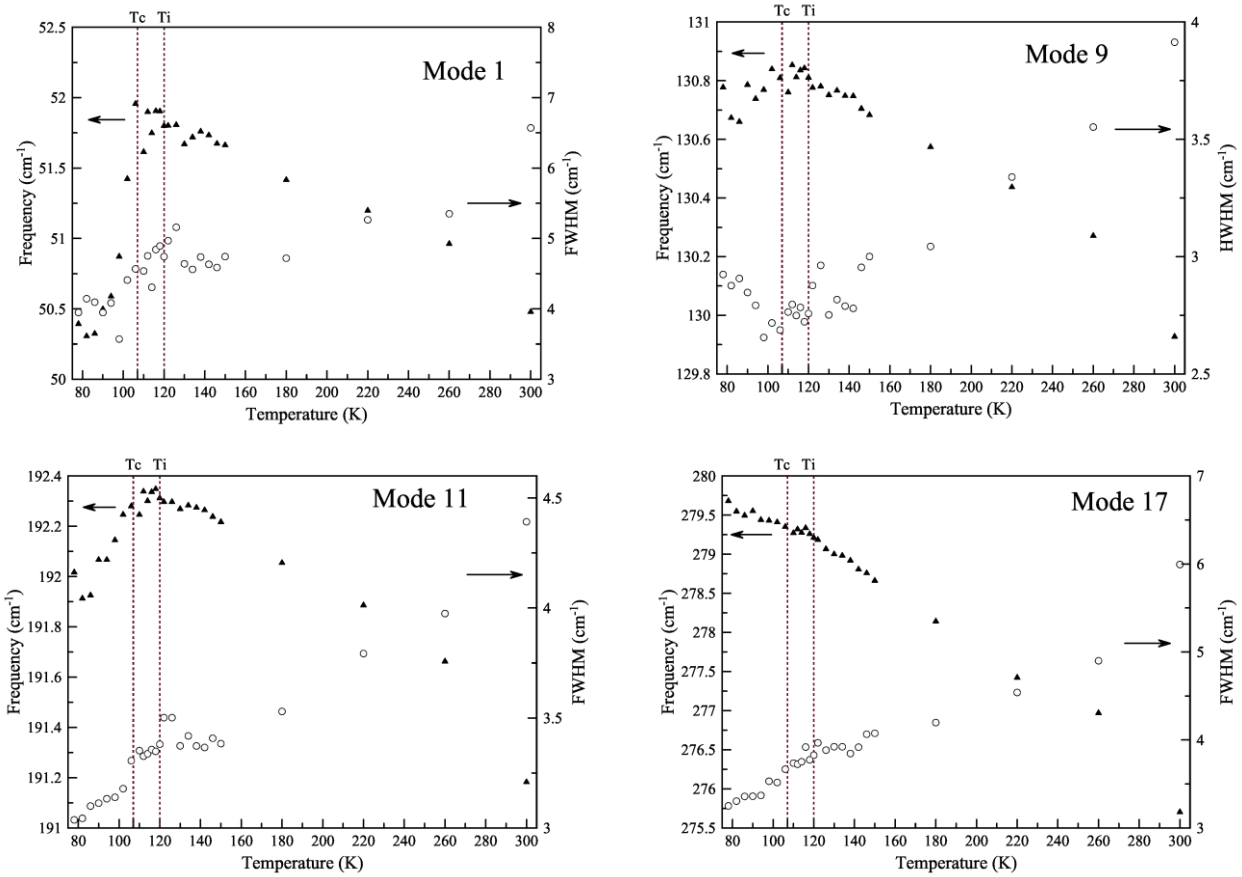

Figure 5.6 Temperature dependence of frequency and width (FWHM) of Raman modes. The numbers correspond to those listed in Table 5.2.

5.3 Polarized Raman scattering spectra of $TlInS_2$

5.3.1 Polarized Raman scattering spectra of $TlInS_2$ at 300 K

As stated by R. Loudon [7], A_g-type phonons should be expected at the diagonal components of the (xx), (yy), and (zz) polarization tensors, while B_g-type phonons are predicted for the (zx), (zy), (xy), and (yz) polarizations. Therefore, when interpreting the crystal symmetry on the assumption of a monoclinic system, it suffices to compare the (xx), (yy), and (zz) spectra with one of the (zx), (zy), (xy), and (yz) spectra. Thus, A_g- and B_g-type phonons should be observed in the $\boldsymbol{x(zz)\bar{x}}$ and $\boldsymbol{x(yz)\bar{x}}$ polarizations, respectively. The Raman spectra of $TlInS_2$ in frequency region 30–400 cm^{-1} at 300 K (paraelectric-N phase) for $\boldsymbol{x(zz)\bar{x}}$ and $\boldsymbol{x(yz)\bar{x}}$ polarization are shown in Figure 5.7a and b, respectively. As in the unpolarized case, each mode in the measurement Raman spectra was deconvoluted into Lorentzian peaks, using a least-squares procedure. The fitting peaks are also shown in Figure 5.7.

We identified the symmetry modes for the $TlInS_2$ crystal as shown in Table 5.3. The Raman spectrum shows 12 phonon modes in the $\boldsymbol{x(zz)\bar{x}}$ geometry, while 15 modes at $\boldsymbol{x(yz)\bar{x}}$. In total, we observed 19 phonons, three more than those reported by K. R. Allakhverdiev et al. [8] for the same frequency range at 300 K. Figure 5.8 shows the temperature dependence of the phonon modes (12–19) in the $\boldsymbol{x(yz)\bar{x}}$ polarization (200–400 cm^{-1}). These modes can be observed in the entire temperature range from 300 to 77 K. This reinforces the deconvolution procedure shown in Figure 5.7.

The symmetry identification, performed according to our data, shows one discrepancy at 48 cm^{-1} with the results obtained in [8]. The small number of observed phonon modes is in agreement with the supposition that the space group of the crysta is $\boldsymbol{C_{2h}^6}$. In this hypothesis, group-theoretical analysis gives 24 Raman actives modes (10 A_g +14 B_g) at the center of the Brillouin zone [7]. Thus, we observed all of the 10 A_g phonons and nine of the 14 B_g phonons predicted.

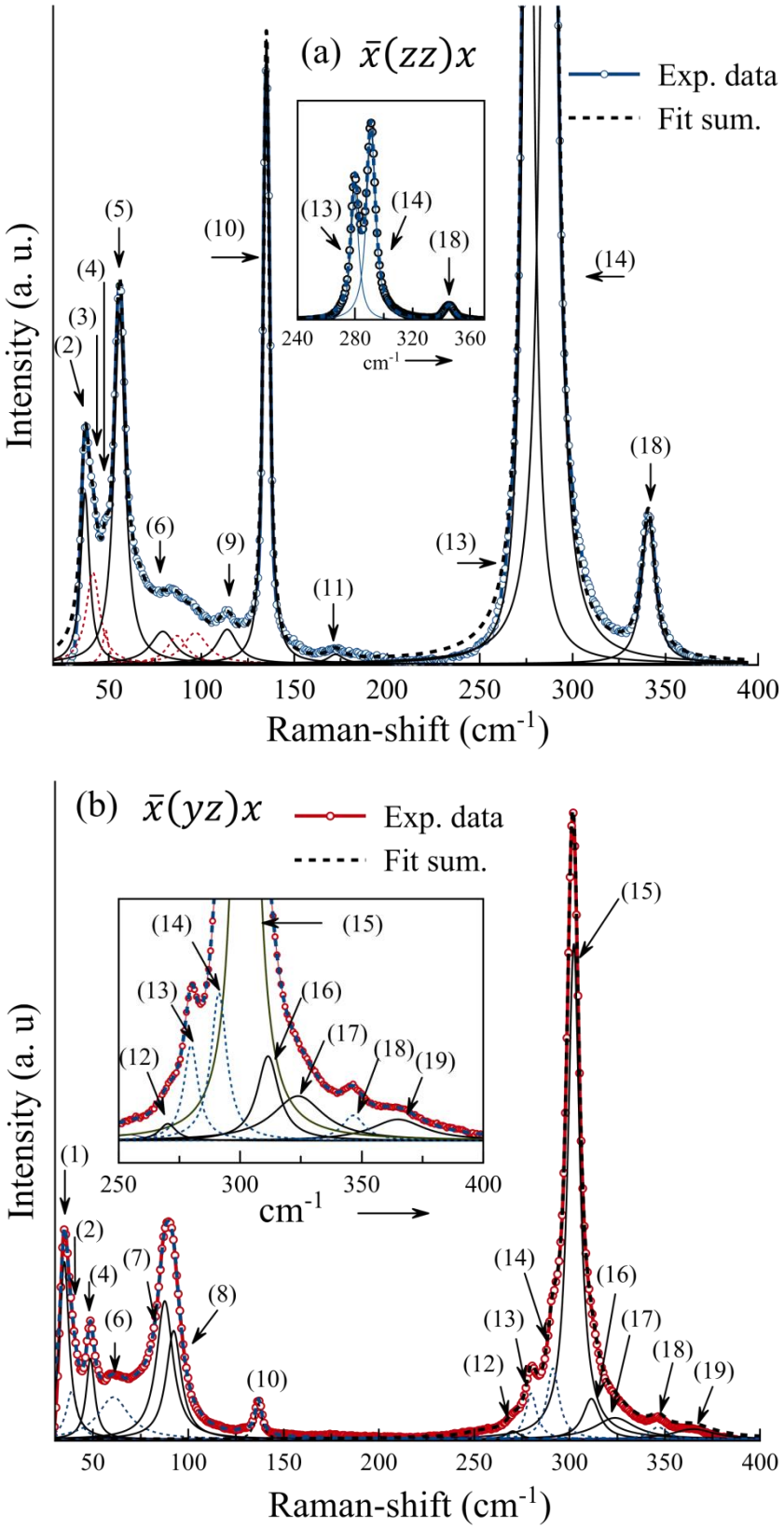

Figure 5.7 Polarized Raman scattering spectra of the $TlInS_2$ crystal at 300 K. (a) A_g-type phonons (black solid line) and B_g-type phonons (red dotted line). (b) B_g-type phonons (black solid line) and, A_g-type phonons (blue dotted line).

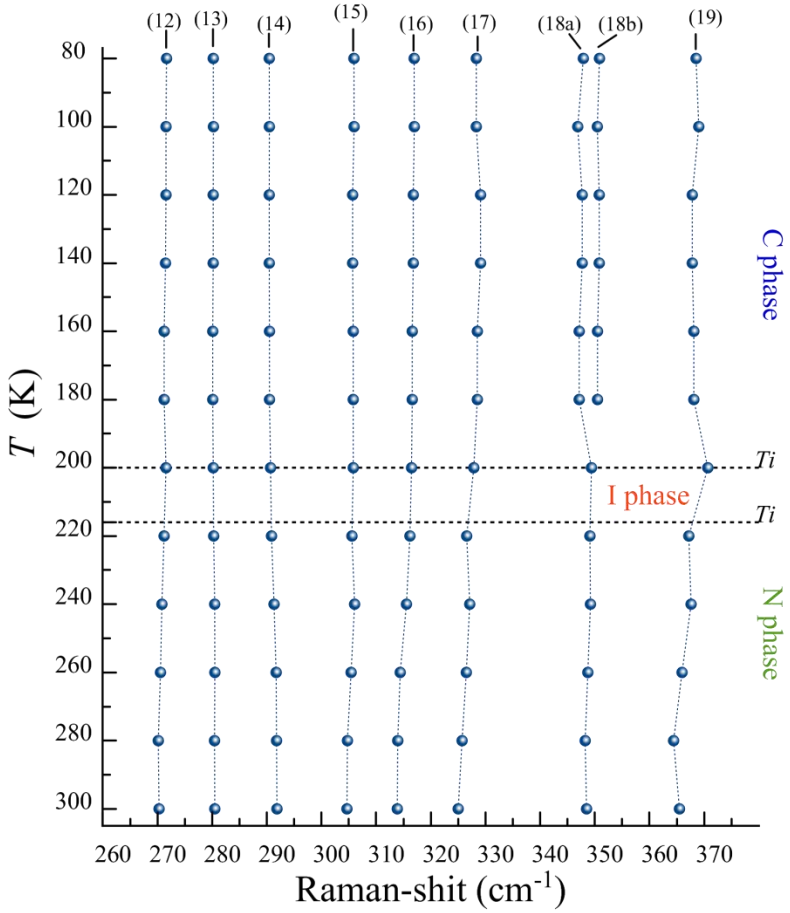

Figure 5.8 Temperature dependence of polarized Raman scattering spectra of the $TlInS_2$ crystal in the $\boldsymbol{x(yz)\bar{x}}$ geometry.

Table 5.3 Mode assignment and phonon frequencies of Raman spectra of $TlInS_2$ crystals at 300 K.

		This work		
Raman line	**Ref. [8]**	$x(zz)\bar{x}$	$x(yz)\bar{x}$	**Mode assignment**
(1)	34 (B_g)	-	34.9	34.9 (B_g)
(2)	37 (A_g)	37.6	37.6	37.6 (A_g)
(3)	43 (A_g)	41.2	-	-
(4)	49 (A_g)	48.7	48.7	48.7 (B_g)
(5)	57 (A_g)	56.4	-	-
(6)	81 (A_g)	77.5	77.5	77.5 (A_g)
(7)	87 (B_g)	86.5	87.5	87.5 (B_g)
(8)	98 (B_g)	96.9	92.3	92.3 (B_g)
(9)	115 (A_g)	114.8	-	-
(10)	137 (A_g)	136.7	136.8	136.8 (A_g)
(11)	-	176.5	175.7	175.7 (A_g)
(12)	271 (B_g)	-	270.7	270.7 (B_g)
(13)	279 (A_g)	279.8	279.8	279.8 (A_g)
(14)	291 (A_g)	291.1	291.1	291.1 (A_g)
(15)	301 (B_g)	-	300.3	300.3 (B_g)
(16)	304 (B_g)	-	-	-
(17)	-	-	311.4	311.4 (B_g)
(18)	-	-	324.2	324.2 (B_g)
(19)	344 (A_g)	345.4	346.8	346.8 (A_g)
(20)	-	-	368.9	368.9 (B_g)

5.3.2 Temperature dependence of polarized Raman scattering spectra in $TlInS_2$

Figure 5.9 shows the polarized Raman spectra of the $TlInS_2$ crystal in the low-frequency range (35– 180 cm^{-1}) at 77, 150, 200, 216, 250, 300, and 320 K. As we did not observe any appreciable effect of successive thermocycling between the commensurate and normal phases, the results are provided without details regarding their acquisition way (i.e., on cooling or heating). Each mode in the measured Raman spectra was deconvoluted into Lorentzian peaks, using a least-squares procedure. The figure also shows an example of the fitting of the Raman spectrum at 77 K. The bands that were deconvoluted into separate lines are indicated by arrows above the relevant frequency. At least seven Raman peaks can be identified in the spectrum obtained at 300 K and this number rises to 10 at 77 K. This is reflected in Figure 5.10, which displays the temperature dependency of the frequency of each Raman line from 77 up to 300 K. The increase of the temperature leads the typical decrease of the intensity and line broadening of the Raman spectra. Moreover, the appearance of additional Raman lines (3, 5, and 8) is an indication of a structural phase transition at low temperatures [1, 4]. More details on the temperature dependence of the frequency of the Raman lines are provided in Figure. 5.11.

In the case of temperature-induced phase transitions in layered compounds, the external (interlayer) modes responsible for phase transitions are expected to have the strongest temperature dependence, while the internal (intralayer) modes are considered to remain relatively undisturbed [9]. Thus, for $TlMeX_2$ layered compounds the interlayer (Tl-X) modes that include displacements of the Tl^+ atoms that are responsible for phase transitions are expected to have the strongest temperature dependence. From the Raman frequency values of Figure 5.11, we calculated the slope ($\partial \nu_i \,/\, \partial T$) to quantify the temperature dependence of the frequencies (ν_i). The numerical values of the slopes are summarized in Table 5.4. In the N phase, we can clearly observe that the modes responsible for the Raman lines 4, 6, and 10 exhibit a strong temperature dependence of the frequency (the highest slope values). It must also be noted that the intensity of these Raman lines exhibits strong temperature dependence (Figure 5.9). We assume that these modes are associated with the interlayer bonding between Tl and S atoms. Additionally, we identified the four Raman lines 1, 2, 7 and 9 that are possibly related to the intralayer bonding between In and S atoms.

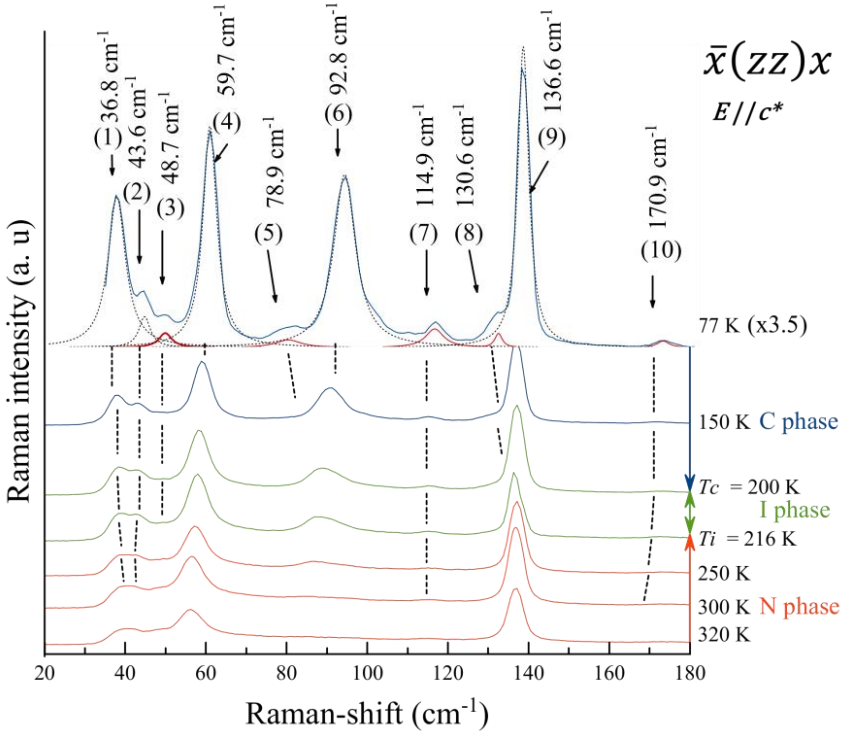

Figure 5.9 Polarized Raman spectra of the $TlInS_2$ crystal in the low-frequency range (35–180 cm^{-1}) at 77, 150, 200, 216, 250, 300, and 320 K.

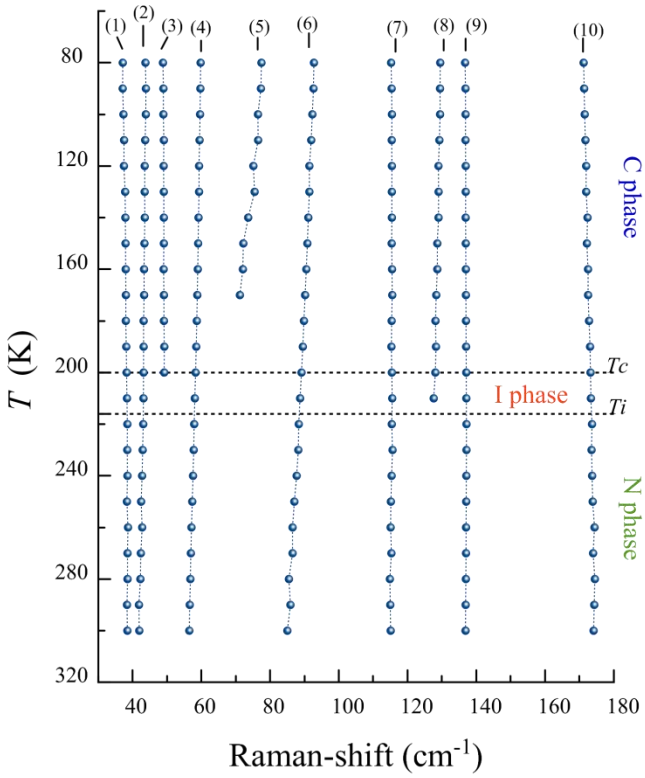

Figure 5.10 Temperature dependence of the Raman line frequencies in the $TlInS_2$ crystal. The dashed lines are visual guides.

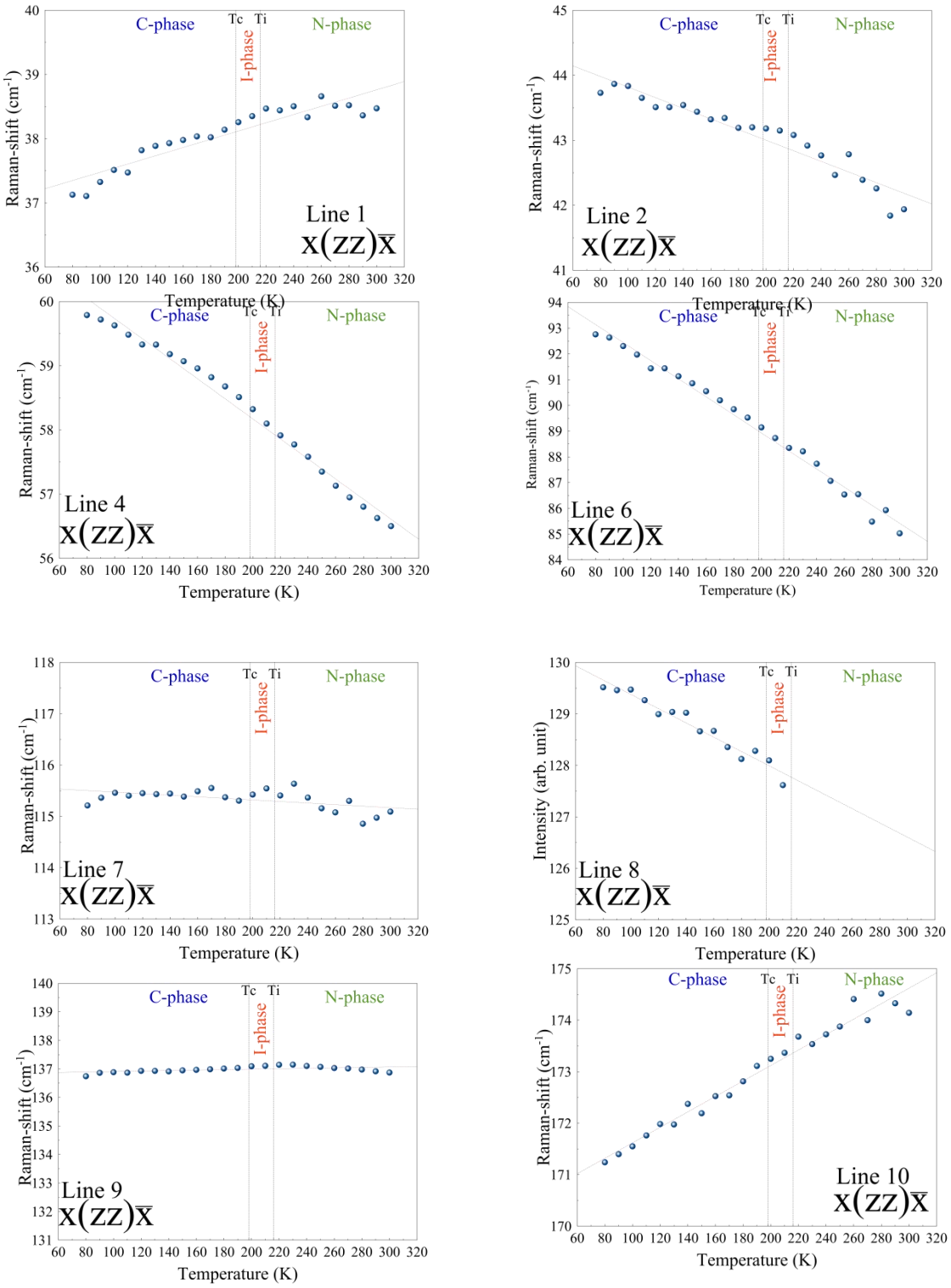

Figure 5.11 Temperature dependence of Raman line frequencies (ν) for each line in the Raman spectra of the $TlInS_2$ crystal. The dashed lines are visual guides.

The intralayer and interlayer Raman modes of the layered compounds $TlGaSe_2$ and $TlGaS_2$ have been determined and reported in [60]. However, as far as we know, there haves been no studies on $TlInS_2$ compounds. Here, we report here the first determination of the intralayer and interlayer Raman modes of layered compound $TlInS_2$.

Table 5.4 Temperature dependence of Raman line frequencies (v_i). The numbers corresponds to those shown in Figures 2 and 3.

Raman line	Slope $(\partial v_i / \partial T)$ x 10^3 cm^{-1} K^{-1}		Type of bonding
	C phase	N phase	
1	6.4		Intralayer
2	-8.2		Intralayer
3	2.3	-	-
4	-15.6		Interlayer
5	-74.1	-	-
6	-35.1		Interlayer
7	-1.5		Intralayer
8	-13.4	-	-
9	0.8		Intralayer
10	15.1		Interlayer

5.4 Summary

The Raman scattering spectra of $TlInS_2$ were analyzed and the temperature dependence of x_0 and γ was obtained. The plots showed the appearance of certain modes with increasing temperature from 77 K. Moreover, irregular behavior was observed in the temperature dependence of the peak positions and lines widths in Figure 5.3. Moreover, we studied the temperature dependence of the frequency and peak width of the Raman lines in $TlGaSe_2$, including the temperature range of the reported ferroelectric phase transition through an intermediate incommensurate phase. Our results in both crystals indicate a complicated situation that cannot be fully explained within the theoretical framework of the phase transitions previous reported for $TlGaSe_2$. Futher studies of the broadening and peak position as a function of the temperature are necessary to fully understand the results obtained in this study.

Moreover, we identified the symmetry modes for the $TlInS_2$ crystal. The Raman spectra shows 12 phonon modes in the $\boldsymbol{x(zz)\bar{x}}$ geometry, while 15 modes in $\boldsymbol{x(yz)\bar{x}}$. In total, we observed 19 phonons, three more than those previously reported for the same frequency range at 300 K. The small number of observed phonon modes is in agreement with the supposition that the space group of the crystal is $\boldsymbol{C_{2h}^6}$. In this hypothesis, group theoretical analysis gives 24 Raman active modes (10 A_g +14 B_g) at the center of the Brillouin zone. Thus, we observed all of the 10 A_g phonons and nine of the 14 B_g phonons predicted. In addition, we studied the polarized Raman spectra of $TlInS_2$ crystals across a wide temperature range that included the reported region of the N-I-C transition. In the $\boldsymbol{x(zz)\bar{x}}$ geometry, we identified three Raman modes that are possibly related to the interlayer bonding between Tl and S atoms and four Raman modes that may be associated to the intralayer bonding between In and S atoms.

References

[1] W. Henkel, H.D. Hochheimer, C. Carlone, A. Werner, S. Ves, and H. G.V. Schnering, Phys. Rev. B, vol. 26, pp. 3211–3221 (1982).

[2] N. M. Gasanly, A. F Goncharov, N. N. Melnik, A. S. Raginov, and V. I. Tagirov, Phys. Stat. Sol. B, vol. 116, pp. 427–443 (1983).

[3] N. S. Yuksek, N. M. Gasanly, and A. Aydinli, J. Raman Spectroscopy, vol. 35, p.55 (2004).

[4] A. Kato, M. Nishigaki, N. Mamedov, M. Yamazaki, S. Abdullaeva, E. Kerimova, H. Uchiki, and S. Iida, J. Phys. Chem. Solids, vol. 64, p. 1713 (2003).

[5] N. S. Yuksek, N. M. Gasanly, and H. Ozkan, J. Korean Phys. Soc., vol. 45, p. 501 (2004).

[6] E. A. Vinogradov, G. N. Zhizhin, N. N. Melnik, S. I. Subbotin, V. V. Panfilov, K. R. Allakhverdiev, E. Yu. Salaev, and R. Kh. Nani, Phys. Status B 95, p. 383 (1979).

[7] K. R. Allakhverdiev et al., Phys. Status Solidi B 152, p. 317 (1989).

[8] R. Loudon, Adv. Phys. 13, pp. 432–482 (1964).

[9] T. Chattopadhyay, C. Carlone, A. Jayaraman, and H. G. V. Schnering, Phys. Rev. B 23, 2471 (1981).

CHAPTER 6

CONCLUSIONS

We investigated the PL spectra of $TlInS_2$ crystals using a confocal microscopy system. For light polarization $\boldsymbol{E} \perp c^*$($\boldsymbol{k}$//c^*), a strong PL band was observed across the entire temperature range from 77 to 300 K, in which a series of phase transitions is believed to occur. At 77 K (ferroelectric-C phase) and under excitation densities above 0.1 MW/cm^2, the PL spectrum consisted of two components: (1) an FE (*H* band) luminescence and (2) biexciton luminescence (*M* band). The binding energy of the biexcitons was estimated to be ~13.5 meV, and the structure dissociated at 160 K. For higher temperatures up to 300 K, the crystal phase underwent a transition from the paraelectric-N -phase through an intermediate I phase, and the PL spectra consisted mainly of FE emission (*H* band). To the best of our knowledge, this is the first observation of biexcitonic emission in the PL spectra of $TlInS_2$ crystals. Furthermore, we investigated the PL spectra of $TlGaSe_2$ using confocal microscopy. The PL spectra appeared only for the $\boldsymbol{k} \perp \boldsymbol{c}^*$ configuration. The spectra, which were asymmetric, were separated into two Gaussian peaks, A and B, located at 2.01 and 2.10 eV, respectively. By analyzing the excitation intensity dependence of the PL intensity and previously reported data, we attributed peak B to pure FE emission from $TlGaSe_2$ crystals. This is the first observation of FE in $TlGaSe_2$ using PL measurements. Peak A was also assigned to FEs; however, it is possible that its FE emission came from crystals in which the ***a*** and ***b*** axis were mixed and exchanged or to layers that were stacked with a parallel shift.

The Raman scattering spectra of $TlInS_2$ were analyzed and the temperature dependence of x_0 and γ was obtained. The plots showed the appearance of certain modes with increasing temperature from 77 K. Moreover, irregular behavior was observed in the temperature dependence of the peak positions and lines widths in Figure 5.3. Moreover, we studied the temperature dependence of the frequency and peak width of

the Raman lines in $TlGaSe_2$, including the temperature range of the reported ferroelectric phase transition through an intermediate incommensurate phase. Our results in both crystals indicate a complicated situation that cannot be fully explained within the theoretical framework of the phase transitions previous reported for $TlGaSe_2$. Futher studies of the broadening and peak position as a function of the temperature are necessary to fully understand the results obtained in this study. The appearance and disappearance of Raman modes and the irregular behavior of the temperature dependence of the Lorentzian parameters may be due to a structural phase transition because the unit cell is quadrupled in direction of the crystallographic $\boldsymbol{c}$ axis. This phenomenon is known as a superlattice. The obtained results are indicative of a complicated picture that is difficult to interpret within the reported theory of phase transitions in $TlInS_2$ and $TlGaSe_2$.

Moreover, we identified the symmetry modes for the $TlInS_2$ crystal, which were in agreement with the supposition that the space group of the crystal is $\boldsymbol{C_{2h}^6}$. In this hypothesis, group-theoretical analysis gives 24 Raman actives modes (10 A_g +14 B_g) at the center of the Brillouin zone. Thus, we observed all of the 10 A_g phonons and nine of the 14 B_g phonons predicted. In addition, we studied the polarized Raman spectra of $TlInS_2$ crystals across a wide temperature range that included the reported region of the N-I-C transition. In the $\boldsymbol{x(zz)\bar{x}}$ geometry, we identified three Raman modes that were possibly related to the interlayer bonding between Tl and S atoms and four Raman modes that could be associated to the intralayer bonding between In and S atoms.

LIST OF PUBLICATION BY THE AUTHOR

Academic papers

1. "Exciton and biexciton luminescence from $TlInS_2$ bulk single crystal"

Raul Paucar, YongGu Shim, Kazuki Wakita, Oktay Alekperov, and Nazim Mamedov, submission to JJAP.

2. "Temperature dependence of low-frequency polarized Raman scattering spectra in $TlInS_2$"

Raul Paucar, YongGu Shim, Kazuki Wakita, Oktay Alekperov, and Nazim Mamedov, submission to Physica Status Solidi.

3. "Temperature dependence of low-frequency optical phonons in $TlInS_2$"

Raul Paucar, YongGu Shim, Kazuki Wakita, Oktay Alekperov, and Nazim Mamedov, Physica Status Solidi (c), Vol 12, Issue 6, 826–829, 2015.

4. "Phase transitions and Raman scattering spectra of $TlGaSe_2$"

Raul Paucar, YongGu Shim, Kazuki Wakita, Oktay Alekperov, and Nazim Mamedov, Journal of Physics: Conference Series, Vol 619, Issue 1, article id. 012018 (2015).

5. "Evaluation of crystal structure in $TlInS_2$ by optical second-harmonic generation".

Kazuki Wakita, Masashi Hagiwara, **Raul Paucar**, YongGu Shim, Kojiro Mimura, and Nazim Mamedov, Conference Series, Vol 619, Issue 1, article id. 012006 (2015).

6. "Excitonic emission of $TlGaSe_2$"

Masashi Hagiwara, **Raul Paucar**, YongGu Shim, Kazuki Wakita, Oktay Alekperov, Arzu Najafov, and Nazim Mamedov, Physica Status Solidi C, Vol 12, Issue 6, 830–833, 2015.

7. "Phase transition and Raman-active modes in $TlInS_2$"

Raul Paucar, Kazuki Harada, Ryoya Matsumoto, Kazuki Wakita, YongGu Shim, Oktay Alekperov, and Nazim Mamedov, Physica Status Solidi C, Vol 10, Issue 7–8, 1132–1135, 2013.

Oral presentations

1. 20th International Conference on Ternary and Multinary Compounds - ICTMC20 (5 - 9 September 2016) MARTIN LUTHER UNIVERSITY, Halle (Saale), Germany. **Raul Paucar**, YongGu Shim, Kazuki Wakita, Oktay Alekperov, and Nazim Mamedov, Raman spectroscopy of optical phonons in $TlInS_2$ layered crystals.

2. 第 76 回応用物理学会秋季学術講演会「2015 年 9 月 13～16 日」愛知県、名古屋市、名古屋国際会場。**Raul Paucar**, YongGu Shim, Kazuki Wakita, Oktay Alekperov, and Nazim Mamedov, Temperature dependence of polarized Raman scattering spectra of $TlInS_2$.

3. 19th International Conference on Ternary and Multinary Compounds – ICTMC19 (1 - 5 September 2014) Toki Messe, Nigata, Japan. **Raul Paucar**, YongGu Shim, Kazuki Wakita, Oktay Alekperov, and Nazim Mamedov, Temperature dependence of low-frequency optical phonons in $TlInS_2$.

4. 第 73 回応用物理学会秋季学術講演会「2012 年 9 月 11～14 日」愛媛県、松山市、愛媛大学。**Raul Paucar**, YongGu Shim, Kazuki Wakita, Oktay Alekperov, and Nazim Mamedov, $TlInS_2$ におけるラマン散乱スペクトルの温度依存性。

5. 18th International Conference on Ternary and Multinary Compounds – ICTMC18 (27 - 31 August 2012) University of Salzburg, Salzburg, Austria. **Raul Paucar**, YongGu Shim, Kazuki Wakita, Oktay Alekperov, and Nazim Mamedov, Phase transition and Raman-active modes in $TlInS_2$.

Poster contributions

1. 応用物理学会フォトニクス分科会第 1 回フォトニクス研究会「2016 年 12 月 2〜3 日」沖縄県青年会館。**Raul Paucar**, YongGu Shim, Kazuki Wakita, Oktay Alekperov, and Nazim Mamedov, $TlInS_2$ 結晶における偏光ラマン散乱スペクトルの温度依存性。

2. 第 77 回応用物理学会秋季学術講演会「2016 年 9 月 13〜16 日」新潟県、新潟市、朱鷺メッセ。**Raul Paucar**, YongGu Shim, Kazuki Wakita, Oktay Alekperov, and Nazim Mamedov, Excitonic emission in β-$TlInS_2$.

3. 20th International Conference on Ternary and Multinary Compounds - ICTMC20 (5 - 9 September 2016) MARTIN LUTHER UNIVERSITY, Halle (Saale), Germany. **Raul Paucar**, YongGu Shim, Kazuki Wakita, Oktay Alekperov, and Nazim Mamedov, Photoluminescence study of $TlInS_2$ using confocal system.

4. 多元系化合物・太陽電池研究会年末講演会「2015 年 12 月 11〜12 日」新潟県長岡市、シティホールプラザ アオーレ長岡 市民交流ホールＡ。**Raul Paucar**, YongGu Shim, Kazuki Wakita, Oktay Alekperov, and Nazim Mamedov, $TlInS_2$ における偏光フォノンスペクトルの温度依存性。

5. 第 76 回応用物理学会秋季学術講演会「2015 年 9 月 13〜16 日」愛知県、名古屋市、名古屋国際会場。**Raul Paucar**, YongGu Shim, Kazuki Wakita, Oktay Alekperov, and Nazim Mamedov, Temperature dependence of polarized Raman scattering spectra of $TlInS_2$.

6. The 5th International Symposium on Organic and Inorganic Electronic Materials and Related Nanotechnologies - EM-NANO (16 - 19 June 2015) Toki Messe, Nigata, Japan. **Raul Paucar**, YongGu Shim, Kazuki Wakita, Oktay Alekperov, and Nazim Mamedov, Low temperature photoluminescence spectra of $TlInS_2$ single crystal.

7. 多元系化合物・太陽電池研究会年末講演会「2014 年 11 月 28 日」京都府、龍谷大学、アバンティ響都ホール。**Raul Paucar**, YongGu Shim, Kazuki Wakita, Oktay Alekperov, and Nazim Mamedov, $TlInS_2$ 結晶における偏光ラマンスペクトラ。

8. 第 75 回応用物理学会秋季学術講演会「2014 年 9 月１７〜２０日」北海道、札幌市、北海道大学。**Raul Paucar**, YongGu Shim, Kazuki Wakita, Oktay Alekperov, and Nazim Mamedov, $TlInS_2$ における低周波数学会フォノンモードの温度依存性。

9. International Conference on Optical, Optoelectronic and Photonic Materials - ICOOPMA (27 July- 1 August 2014) Leeds University, Leeds, UK. **Raul Paucar**, YongGu Shim, Kazuki Wakita, Oktay Alekperov, and Nazim Mamedov, Phase transitions and Raman scattering spectra of $TlGaSe_2$.

10.多元系化合物・太陽電池研究会年末講演会「2013 年 11 月 22～23 日」茨城県、宇宙航空研究開発機構、筑波宇宙センター 総合開発推進棟 大会議室。**Raul Paucar**, YongGu Shim, Kazuki Wakita, Oktay Alekperov, and Nazim Mamedov, Phase transitions and Raman-active modes in $TlGaSe_2$。

11. 多元系化合物・太陽電池研究会」年末講演会「2011 年 12 月 9～10 日」愛媛県、松山市、愛媛大学。Raul Paucar, YongGu Shim, Kazuki Wakita, Oktay Alekperov, and Nazim Mamedov, Raman Scattering in $TlInS_2$.

12. 第 72 回応用物理学会秋季学術講演会「2011 年 8 月 29 日～9 月 2 日」山形県、山形市、山形大学、小白川キャンパス。**Raul Paucar**, YongGu Shim, Kazuki Wakita, Oktay Alekperov, and Nazim Mamedov, Raman Scattering in $TlInS_2$.

ACKNOWLEDGMENTS

I would like to express my sincere gratitude to my supervisor, Prof. Dr. Kazuki Wakita, for his technical support, continual guidance, and enthusiasm and for providing me with an excellent atmosphere for doing research.

I would like to thank my thesis committee members: Prof. Hideo Muro, Prof. Hidekaz Yamamoto, Prof. Susumu Suzuki, and Prof. Koji Suizu for all their guidance through this process; your discussion, ideas, and feedback have been absolutely invaluable.

My sincere thanks also go to Prof. Nazim Mamedov, Prof. Oktay Alekperov, and Prof. YongGu Shim for their technical support.

Finally, and most importantly, I am very thankful to my parents Manuel and Rosa, for their unwavering love and support.